Quantitative Multilevel Analysis of Central Metabolism in Developing Oilseeds of Oilseed Rape during in Vitro Culture[1][OPEN]

Jörg Schwender, Inga Hebbelmann, Nicolas Heinzel, Tatjana Hildebrandt, Alistair Rogers, Dhiraj Naik, Matthias Klapperstück, Hans-Peter Braun, Falk Schreiber, Peter Denolf, Ljudmilla Borisjuk, and Hardy Rolletschek*

Brookhaven National Laboratory, Biological, Environmental, and Climate Sciences Department, Upton, New York 11973 (J.S., I.H., A.R., D.N.); Department of Molecular Genetics, Leibniz Institute of Plant Genetics and Crop Plant Research, D–06466 Gatersleben, Germany (N.H., L.B., H.R.); Institut für Pflanzengenetik, Universität Hannover, 30419 Hannover, Germany (T.H., H.-P.B.); Department of Environmental Science, Indian Institute of Advanced Research, Koba, Gandhinagar 382007, Gujarat, India (D.N.); Clayton School of Information Technology, Monash University, Melbourne, Victoria 3800, Australia (M.K., F.S.); Institute of Computer Science, University Halle-Wittenberg, 06120 Halle, Germany (F.S.); and Bayer CropScience, 9052 Zwijnaarde, Belgium (P.D.)

ORCID IDs: 0000-0002-1226-2337 (D.N.); 0000-0002-4459-9727 (H.-P.B.); 0000-0003-4567-2700 (P.D.).

Seeds provide the basis for many food, feed, and fuel products. Continued increases in seed yield, composition, and quality require an improved understanding of how the developing seed converts carbon and nitrogen supplies into storage. Current knowledge of this process is often based on the premise that transcriptional regulation directly translates via enzyme concentration into flux. In an attempt to highlight metabolic control, we explore genotypic differences in carbon partitioning for in vitro cultured developing embryos of oilseed rape (*Brassica napus*). We determined biomass composition as well as 79 net fluxes, the levels of 77 metabolites, and 26 enzyme activities with specific focus on central metabolism in nine selected germplasm accessions. Overall, we observed a tradeoff between the biomass component fractions of lipid and starch. With increasing lipid content over the spectrum of genotypes, plastidic fatty acid synthesis and glycolytic flux increased concomitantly, while glycolytic intermediates decreased. The lipid/starch tradeoff was not reflected at the proteome level, pointing to the significance of (posttranslational) metabolic control. Enzyme activity/flux and metabolite/flux correlations suggest that plastidic pyruvate kinase exerts flux control and that the lipid/starch tradeoff is most likely mediated by allosteric feedback regulation of phosphofructokinase and ADP-glucose pyrophosphorylase. Quantitative data were also used to calculate in vivo mass action ratios, reaction equilibria, and metabolite turnover times. Compounds like cyclic 3′,5′-AMP and sucrose-6-phosphate were identified to potentially be involved in so far unknown mechanisms of metabolic control. This study provides a rich source of quantitative data for those studying central metabolism.

Seeds develop by absorbing nutrients from their mother plant and using these to synthesize a combination of starch, protein, and lipid. The size and number of seeds that finally develop determine the crop's yield, while their composition determines the end-use quality of the crop. The conversion of nutrients into storage products involves a complex network of metabolic reactions, many of which are subject to transcriptional, translational, and posttranslational regulation. Attempting to engineer seed composition clearly requires a firm understanding of these regulatory networks.

The seed's central metabolism differs markedly from those of both a photosynthesizing leaf and a root. In most species, the immature seed is green for a period during its development, so during this phase it is regarded as being photoheterotrophic. A further level of complexity arises as a result of spatial heterogeneity within the seed (Rolletschek et al., 2011; Borisjuk et al.,

2013a), which generates a significant degree of metabolic heterogeneity. Thousands of genes are involved in seed development. In Arabidopsis (*Arabidopsis thaliana*), about 17,500 distinct mRNAs (approximately 60% of the full gene complement) are transcribed in the seed during its development, with about 1,300 of these being seed specific (Belmonte et al., 2013). While this set of genes no doubt provides a full picture of the stage- and tissue-specific framework of gene activity, many examples have been described in plants where the pairs of transcript versus protein or protein versus flux are rather discordant (Junker et al., 2007; Hajduch et al., 2010; Fernie and Stitt, 2012; Schwender et al., 2014). Thus, monitoring of gene expression is not sufficient to define metabolic activities in vivo. Posttranscriptional regulation seems to be of particular relevance for the control of metabolic flux. Major mechanisms in play are protein modification (Finkemeier et al., 2011; Meyer et al., 2012) and allosteric enzyme regulation (Plaxton and Podestá, 2006). A systems-level approach is needed to unravel such a level of complexity. A suggested start involves metabolic modeling to provide a quantitative view of seed metabolism (Schwender, 2008). In microbes, this approach has already helped to identify targets for molecular engineering and to suggest improved engineering strategies (Pickens et al., 2011).

Oil crops like soybean (*Glycine max*), oilseed rape (*Brassica napus*), and sunflower (*Helianthus annuus*) accumulate 20% to 60% of dry weight oil in the form of triacylglycerol (TAG) in their seeds but also significant amounts of proteins and sometimes starch. Substantial diversity is observed in TAG structure, rate of oil synthesis, and level and spatial pattern of accumulation (Durrett et al., 2008; Baud and Lepiniec, 2009, 2010; Borisjuk et al., 2013b). The biochemical machinery of oil synthesis has been well characterized (Rawsthorne, 2002). Numerous comparative transcriptome studies of oil-accumulating plant tissues have given important additional insights into the regulation of TAG synthesis (Ruuska et al., 2002; Bourgis et al., 2011; Troncoso-Ponce et al., 2011). Metabolic flux studies with developing seeds have added a quantitative understanding of in vivo pathway usage in oilseeds (O'Grady et al., 2012). To modulate seed oil levels or composition, various attempts have been chosen, mostly relying on introducing specific enzymes (Weselake et al., 2008; Kelly et al., 2013) or metabolite transporters (Fuchs et al., 2013; Kim et al., 2013). A number of seed-specific transcription factors are known to affect oil storage capabilities (Le et al., 2010); their modulated expression as well as the introduction of engineered transcription factors can enable a more global modulation of oilseed metabolism (Century et al., 2008; Gupta et al., 2012; Singh et al., 2013). However, despite past progress based on the multiple complementary molecular genetic and biochemical studies in various oilseed species, our understanding of and ability to manipulate seed composition are still very limited.

Here, the distribution of flux control in carbon partitioning in oilseeds should be relevant. Although the modulation of individual glycolytic steps can have significant effects on oil accumulation (Lonien and Schwender, 2009; Guo et al., 2014), the lesson learned from many attempts to alter pathway flux by the manipulation of single enzyme steps tends to be that allosteric control mechanisms will cause evasive behavior of the system (Morandini, 2009). Thus, quantitative, system-wide studies are needed to unravel the mechanisms of flux distribution and control in seed central metabolism.

Here, a combination of targeted metabolomics, proteomics, enzyme activity profiling, ^{13}C-based metabolic flux analysis (MFA), and computational analysis is described as part of an attempt to understand the regulation of central metabolism of the developing plant seed. As a model species, we have chosen oilseed rape, being a close relative to the model plant Arabidopsis and a leading temperate oilseed crop of high economic value. In particular, while many studies infer metabolism in oilseeds on a molecular genetic level, the aim here was to explore the significance of metabolic control. For such integrative analysis, the measurement of metabolic flux (^{13}C-based MFA) is of central importance (Fernie et al., 2005); therefore, we chose in vitro embryo culture as an experimental system that has been used successfully before in multiple biochemical and ^{13}C-based MFA studies (Schwender and Ohlrogge, 2002; Schwender et al., 2003, 2004, 2006; Goffman et al., 2005; Junker et al., 2007). Given the practical limitations associated with extending a high-intensity systems biology approach to several hundred accessions, an initial screen was conducted to identify a diverse panel of materials that contrasted with respect to their embryo composition. The experimental strategy taken (Fig. 1) was based on the outcomes of a previous field trial (http://documents.plant.wur.nl/cgn/pgr/brasedb/brasresgen.htm) where the performance of a selection of *Brassica* spp. accessions was documented; these data led to the selection of a panel of 63 oilseed rape accessions (henceforth called entries) varying widely with respect to their seed composition and weight. In this study, this set of entries was rescreened to identify a subset of seven entries representing wide-ranging genotypic variation for in vitro embryo biomass composition as well as embryo growth rates. To this set, we added another two genotypes: a transgenic oilseed rape line engineered to overexpress in its seeds a gene encoding the enzyme DIACYLGLYCEROL ACYLTRANSFERASE1 (DGAT1) from Arabidopsis and a reference line representing its genetic background. Transgenic oilseed rape lines overexpressing DGAT1, encoding an enzyme catalyzing the formation of triglycerides from diacylglycerol and acyl-CoA, have been reported to feature an elevated lipid content in seeds (Weselake et al., 2008). Altogether, comparison of the nine genotypes by our multiomics approach presented here led to the identification of potential regulators, regulatory mechanisms, and markers of seed metabolism.

Figure 1. Experimental strategy for quantitative analysis of seed metabolism. *, Unit conversion to a common volume basis was based on the density of embryo tissue (1.2 mg fresh weight [FW] mL^{-1}), a ratio of fresh weight to dry weight (DW) of 2, and the metabolically active volume of the embryo tissue being 33% of the total volume. GC, Gas chromatography; IEF, isoelectric focusing.
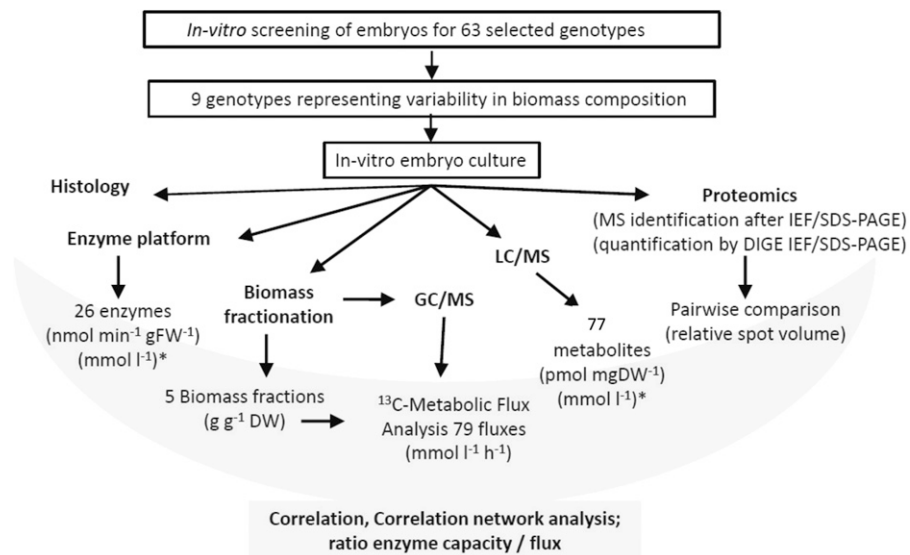
RESULTS

In Vitro Screening Identified Entries Contrasting for Growth Rate and Embryo Composition

Developing embryos of 63 oilseed rape entries were dissected from growing plants and cultured in vitro under uniform conditions (see "Materials and Methods"). After 10 d of culture, embryos of the 63 oilseed rape entries were similar with respect to their morphology but varied in size. Histological analysis revealed that the plastids in the cytoplasm present in the small embryos typically contained one or two small starch grains along with numerous lipid bodies (Fig. 2). In contrast, the plastids in the cytoplasm of large embryos harbored large aggregates of starch grains, along with a substantial vacuole and few and smaller lipid bodies. A subsequent analysis of fresh and dry weights, total lipid content, fatty acid composition, and total protein content (Supplemental Table S1) confirmed the variation in embryo composition indicated by microscopy. In particular, the lipid content varied by a range of about 14% (total lipid on a dry weight basis) between genotypes. Based on contrasting embryo weight, lipid content, and lipid-protein ratio, seven entries (BCS1875, CR2277, CR3231, CR3135, BCS1859, CR2186, and CR3217) were selected to represent the range of variation present in the 63 entries (Supplemental Table S2). Their embryos, along with those of the *DGAT1*-overexpressing transgenic line (DGAT) and the corresponding control plant (oilseed rape [OSR] reference line), were cultured in bulk for subsequent analyses.

Parallel Determination of Flux, Metabolite Concentration, and Enzyme Activity

Figure 1 gives an overview of the analysis. In short, developing embryos of the nine selected entries were cultured in vitro in the presence of ^{13}C-labeled Glc, and

flux distributions were determined for all nine entries using ^{13}C-based MFA (Supplemental Methods S1), resulting in 79 net fluxes of central metabolism across all nine oilseed rape entries (Supplemental Table S3G). Embryos were cultured in parallel under the same conditions in three replicates, and the activities of 26
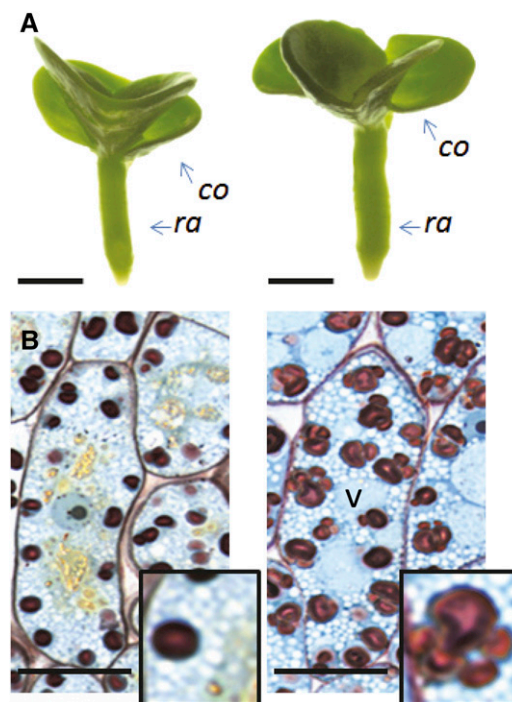
Figure 2. The architecture and ultrastructure of the oilseed rape embryo cultured in vitro for 10 d. A, Embryo architecture in high-lipid (CR3217) and low-lipid (CR2186) entries. co, Cotyledon; ra, radicle. B, Storage parenchyma cells of the same two entries. Nuclei, vacuole (V), lipid bodies, and cell wall were all visualized by Toluidine Blue staining. The intensely stained structures are starch grains. Insets show individual starch grains surrounded by lipid bodies. Bars = 1 mm (A) and 10 μm (B).

key metabolic enzymes were determined by measurement of the total extractable activity. The enzymes were assayed under optimized conditions under substrate saturation, and the values represent estimates of their peak in vivo catalytic capacities (V_{max}; Supplemental Table S4A). In addition, the use of the liquid chromatography (LC)-mass spectrometry (MS) platform enabled the quantification of 77 metabolite intermediates across all nine entries (the full metabolite data set is given in Supplemental Table S5A). The data sets for biomass fractions (Supplemental Fig. S1), fluxes, enzymes, and metabolite concentrations were combined into 187 measurements (Supplemental Table S6B) and compared between the genotypes based on Pearson correlation. The resulting 187 × 187 matrix of pairwise correlations (Supplemental Table S6C) contained 3,757 significant correlations ($P \le 5\%$; Supplemental Table S6, C and D; Supplemental Fig. S2). Furthermore, proteomic analysis of the nine entries was done based on five pairwise comparisons (Supplemental Table S7).

Tradeoff between Starch and Lipids across the Nine Oilseed Rape Entries

As part of ^{13}C-based MFA, biomass fractions of embryos of all nine test entries were determined (Supplemental Table S2; Supplemental Fig. S1). In all genotype entries, lipid was the most abundant biomass compound (Supplemental Fig. S1). Across the entries, the largest change in biomass proportions was for the starch fraction, ranging from 3% to 22% (w/dry weight), followed by lipid, protein, cell wall, and free metabolite fractions (ranging from 25%–37%, 14%–23%, 14%–19%, and 18%–22%, respectively). Significant correlations between the biomass fractions ($P < 5\%$) were found for lipid and starch ($R = -0.90$) and for starch and protein ($R = -0.73$). Altogether, across the entries, the change in embryo composition can be described as a tradeoff of starch against lipid and protein. With starch and lipid being the most abundant fractions and having the largest variability and highest correlation across the entries, the interpretation of the other data sets will be mostly in consideration of a lipid/starch tradeoff.

Correlation Networks Are Indicative of Multilayered Control of Carbon Partitioning

Between the five biomass components and the enzymes, metabolites, and fluxes, there were 165 significant correlations (Supplemental Table S6D). To focus on the dominant starch/lipid tradeoff, Figure 3 shows all measurements that significantly correlate to starch or lipid content (significance for $R \ge 0.66$). The starch network is considerably larger than the lipid network, and there are both positive and negative correlations (Fig. 3, color coding of nodes around the biomass center nodes). Between the nodes in Figure 3, there are
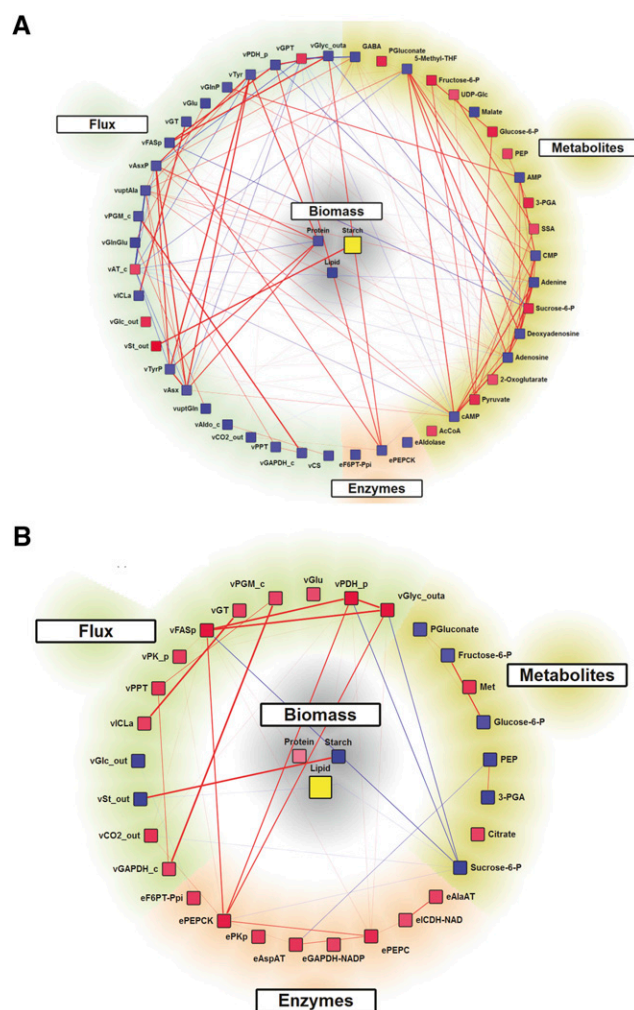
Figure 3. Correlation network analysis for the developing seed. Correlation of flux, metabolite abundance, and enzyme activity values with starch (A) or lipid (B) content is shown. Networks are defined by thresholding Pearson correlation coefficients ($R \ge 0.66$). Positive and negative correlations are coded by red and blue, respectively. The color of the nodes indicates correlation to starch (A) or lipid (B). Only strong correlations between nodes ($R \ge 0.9$) are shown as edges with thickness weighted by R.

624 and 255 significant correlations (edges; shown only for $R \ge 0.9$). The starch network is highly connected, with an edge:node ratio of 12.2. For the smaller lipid network, the edge:node ratio is 8. Altogether, Figure 3 highlights that there are strong correlations between fluxes, metabolites, and enzymes, suggesting multilayered control of carbon partitioning between lipids and starch. In the following, we further explore the different experimental data sets.

Coordination of Central Metabolism Flux with Change in Biomass Composition

Across the nine entries, there were 83 significant correlations ($P \le 5\%$) between the biomass components and the 79 fluxes (Supplemental Table S6, C and D).

A representative flux distribution in the central metabolism of entry OSR reference line is shown in Figure 4. Effluxes into accumulating biomass compounds are shown in red, since they are directly derived from the biomass proportions. Across the entries, fluxes into lipid and starch are negatively correlated ($R = -0.75$), and each of them, in turn, is highly correlated to a number of internal fluxes (Table I). Flux through de novo synthesis of fatty acids is positively correlated to Glc uptake and glycolytic reactions (Table I, vuptGlucose, vHex_HPc, and vPKp), and across the entries the conversion of Glc via PEP and pyruvate into fatty acids is of predominant flux magnitude. A preference for cytosolic over plastidial glycolysis (Fig. 4) was common to all entries and has

been proposed from an analysis of transcriptomic data (Troncoso-Ponce et al., 2011). In addition to glycolysis, fatty acid synthesis is also fed by an alternative sugar catabolic pathway. Figure 4 shows substantial carbon flux via the Rubisco shunt (vRubp), which is characteristic for all entries (Table II). Yet, across the entries, the flux via this light-dependent shunt (Schwender et al., 2004) is rather invariable and not significantly correlated to fatty acid synthesis. Apart from glycolysis and the Rubisco shunt, hexose phosphates can be consumed by the OPPP, which generates NADPH for reductive processes, in particular for fatty acid biosynthesis. Across the nine entries, the cytosolic flux through OPPP (vG6PDHc) was about 1 order of magnitude higher than in the plastidial one (vG6PDHp).
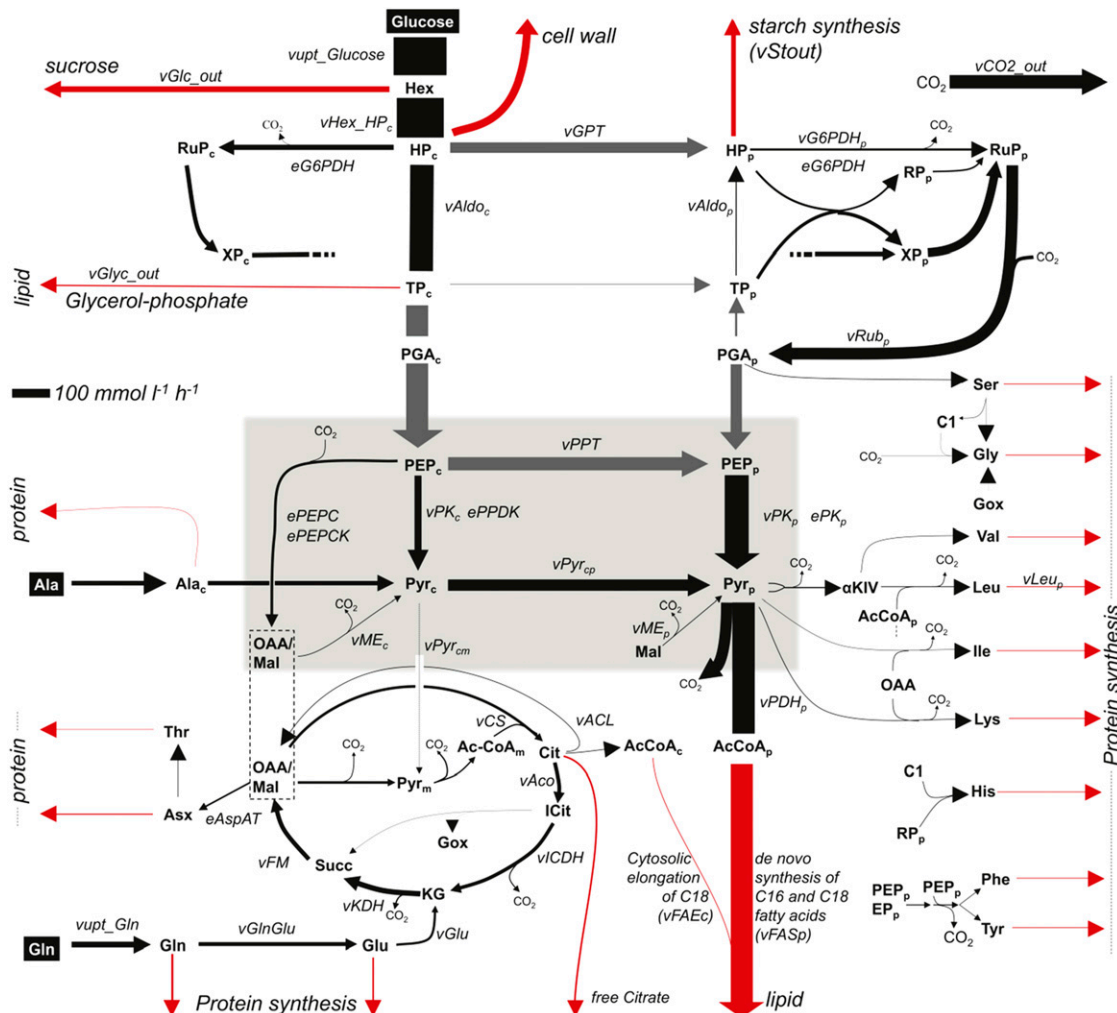
Figure 4. Metabolic flux map of the entry OSR reference line, representative for the flux distributions across the nine entries (Supplemental Table S3G). Carbon net flux is indicated by the thickness of the arrows. Red arrows indicate carbon flux drains into end-product accumulation (lipid, protein, and starch), and gray arrows indicate statistically weakly determined flux values. The compartmentalized phospho*enol*pyruvate (PEP)/pyruvate node is highlighted in orange. c, Compartment-specific enzyme isoform or flux (cytosol); p, compartment-specific enzyme isoform or flux (plastid); cm, transport cytosol to mitochondria; cp, transport cytosol to plastid. For abbreviations for reactions and enzymes, see Table I. For a list of metabolite abbreviations used, see Supplemental Table S3C.

Table I. *Selected significant flux and enzyme activity correlations across the nine oilseed rape entries (+ or − correlations) for values of net fluxes*

All listed correlations are significant at the 2% level ($P < 2\%$; see also Fig. 4 and Supplemental Table S6C). e, Enzyme activity; v, metabolic flux; c, compartment-specific enzyme isoform or flux (cytosol); p, compartment-specific enzyme isoform or flux (plastid).

Selected Biomass Flux	Correlation to	Flux/Enzyme Name[a]	R
De novo synthesis of C16 and C18 fatty acids ($vFAS_p$)	Flux of glycerol into TAG	vGlyc_out	1.00[b]
	Plastidic pyruvate dehydrogenase	$vPDH_p$	1.00
	Plastidic pyruvate kinase (PK_p)	vPK_p	0.92
	CO_2 efflux	vCO2_out	0.90
	Glucokinase and fructokinase	$vHex\_HP_c$	0.87
	Glc uptake	vuptGlucose	0.82
	Plastidic oxidative pentose phosphate pathway (OPPP)	$vG6PDH_p$	0.78
	Phospho*enol*pyruvate carboxylase (PEPC)	ePEPC	0.90
	PEP carboxykinase	ePEPCK	0.98
	PK_p	ePK_p	0.85
	Asp aminotransferase	eAspAT	0.86
Cytosolic elongation of C18 fatty acids ($vFAE_c$)	ATP:citrate lyase	vACL	1.00[b]
	Transport of pyruvate into mitochondria	$vPyr_{cm}$	0.98
	Mitochondrial pyruvate dehydrogenase, citrate synthase	vCS	0.89
	Isocitrate dehydrogenase	vICDH	−0.80
	Aconitate hydratase	vAco	−0.78
	Plastidic PFK, Fru-1,6-bisP aldolase	$vAldo_p$	−0.77
	Cytosolic PFK, Fru-1,6-bisP aldolase	$vAldo_c$	0.77
	Glc-6-P dehydrogenase	eG6PDH	−0.77
	Pyruvate, phosphate dikinase	ePPDK	0.85
Starch synthesis (vStout)	Gln uptake	vuptGln	−0.82
	Net conversion of Gln to Glu by various reactions that interconvert Gln and Glu	vGlnGlu	−0.82
	Net conversion of hexose into Suc	vGlc_out	0.81
	Cytosolic Fru-1,6-bisP aldolase	$vAldo_c$	−0.79
	Reactions with interconversion of Glu and 2-oxoglutarate	vGlu	−0.79
	CO_2 efflux	vCO2_out	−0.76
	Glc-6-P translocation of cytosol/plastid	vGPT	0.76
	Plastidic pyruvate dehydrogenase	$vPDH_p$	−0.75

[a]As seen in Figure 4.   [b]Correlation predefined by network stoichiometry.

vG6PDHp was positively correlated with plastidial fatty acid synthesis (Table I), suggesting its importance for lipid synthesis.

In the lower part of glycolysis, PEP is mostly converted to pyruvate via PKp and PKc (Fig. 4) and to a minimal extent via the oxaloacetate/malate bypass (i.e. via a three-enzyme sequence of PEPC, malate dehydrogenase, and malic enzyme [see highlighted subnetwork in Fig. 4]). Across the entries, PEPC flux was only 4% to 7% of the flux into fatty acids, while 50% to 70% of the plastidial pyruvate entering fatty acid synthesis was generated via PKp (Table II). vPKp was positively correlated with the flux into fatty acid synthesis (Table I), and remarkably, the PKp enzyme activity was positively correlated as well (see below), suggesting that PKp exerted a strong measure of control over fatty acid synthesis and lipid content.

Apart from the de novo synthesis of fatty acids in the plastid, C18 fatty acids can also be further elongated via a cytosolic elongation system that requires acetyl-CoA derived from citrate by a cytosolic ATP:

citrate lyase activity (Fig. 4, vACL). Across the nine entries, there was substantial variability for the flux into the fatty acid cytosolic elongation (vFAEc; i.e. the formation of C20 or C22 chains, in particular erucic acid). Six of the nine entries of our study are considered zero erucic acid oilseed rape cultivars. This genetic trait found in various oilseed rape cultivars is considered to be caused by a mutation in an enzyme of cytosolic fatty acid elongation (FATTY ACID ELONGASE1; Wu et al., 2008). The flux correlations in Table I indicate that increased flux of vFAEc is achieved by a concomitant increase in citrate synthesis; that is, the higher transfer of pyruvate from cytosol to the mitochondria (vPyr_cm) was achieved by an increase in mitochondrial pyruvate dehydrogenase and citrate synthase flux (vCS) as well as by the decreased consumption of citrate in the tricarboxylic acid cycle by aconitase/isocitrate dehydrogenase (vICDH; Fig. 4). Regardless of this variation in tricarboxylic acid cycle flux, the tricarboxylic acid cycle-related fluxes were all relatively small across all entries: while

Table II. *Relative fluxes across the nine oilseed rape entries*

c, Compartment-specific enzyme isoform or flux (cytosol); p, compartment-specific enzyme isoform or flux (plastid).

Parameter	BCS1875	CR2277	CR3231	CR3135	BCS1859	DGAT	OSR Reference Line	CR2186	CR3217	Average
						%				
Carbon conversion efficiency[a]	84	86	86	83	84	80	80	80	79	82 ± 03
Relative Rubisco flux[b]	68	59	32	62	59	51	42	51	46	52 ± 11
PEP-consuming reactions relative to flux into plastidic fatty acid synthesis ($vFAS_p$)										
PKp (vPKp)	62	54	71	72	74	74	72	67	71	69 ± 7
Cytosolic pyruvate kinase (PKc; vPKc)	28	42	27	20	19	18	21	24	26	25 ± 7
PEPC (vPEPC)	7	6	4	6	6	5	6	6	6	6 ± 1
NADPH production by OPPP relative to NADPH consumption by plastidic fatty acid synthesis ($vFAS_p$)[c]										
NADPH by plastidic OPPP	2	0	0	5	3	9	7	5	2	4 ± 3
NADPH by plastidic and cytosolic OPPP	47	11	0	50	37	39	25	62	51	36 ± 20

[a]Percentage of total carbon uptake being stored in biomass. [b]3-Phosphoglyceric acid (3-PGA) generated by Rubisco. [c]NADPH production: $2 \times$ OPPP flux (two NADPHs per molecule of Glc-6-P oxidized). NADPH consumption is based on fatty acid biosynthetic flux (vFASp), considering the fatty acid chain length distribution and distinguishing cytosolic fatty acid synthesis. Per elongation cycle of an acyl chain, one NADPH and one NADH are required for plastidic fatty acid synthase and two NADPHs are required for cytosolic elongase.

fatty acid synthesis flux ranged between 96 and 133 mmol L^{-1} h^{-1} (Supplemental Table S3G), the absolute values for vCS, vFM, vICDH, and vKDH ranged between 0.1 and 13.6 mmol L^{-1} h^{-1}. Fluxes through the mitochondrial, cytosolic, and plastidial isoforms of malic enzyme (vMEm, vMEc, and vMEp) were similarly small, again indicating that the formation of pyruvate through malic enzyme makes only negligible contributions to fatty acid synthesis.

The Peak Catalytic Activities of Several Enzymes Correlate with the Biomass Components and Are above Pathway Flux

Across the nine entries there are seven significant correlations ($P \leq 5\%$) between the biomass components and the 26 assayed enzyme activities (Supplemental Table S6, C and D). The activities of four glycolysis-associated enzymes (pyrophosphate-dependent phosphofructokinase [PFP], PKp, PEPC, and PEP carboxykinase) and that of Asp transaminase were positively correlated with the proportion of lipid present in the embryo (Supplemental Table S6C). Four of these enzyme activities also had strong positive correlation to de novo synthesis of fatty acids (Table I).

For 19 of the 26 measured enzyme activities, we could derive a comparison of enzyme capacity (V_{max}) with the magnitude of enzyme-related fluxes (V_{max}-flux ratio; Table III). Ratios were computed by taking into consideration subcellular compartmentation and activities of isoenzymes. For example, since cytosolic and plastidic enolase activities were captured by one assay, enolase activity was compared with the sum of cytosolic and plastidic flux magnitudes (Table III). For most of the ratio determinations, V_{max} was in excess of net flux by about 1 to 5 orders of magnitude. This is not unexpected, given that most enzymes are thought to operate at subsaturation in vivo (Plaxton, 2004) and that, for enzymes operating close to the chemical

equilibrium, a large surplus of enzyme activity is required to sustain a net flux in one direction (Morandini, 2009). In addition, allosteric inhibition might have a strong impact on in vivo activity. PEPC and PKc, for example, are known to be under complex allosteric feedback control (Moraes and Plaxton, 2000; Smith et al., 2000). However, for ADP-glucose pyrophosphorylase (AGPase) and enolase, the V_{max}-flux ratio was close to unity (Table III). Therefore, pathway flux through these reactions could be limited by the amount of enzyme activity present. In the case of AGPase, estimation of the in vivo mass action ratio (Table IV) suggests that the reaction is far removed from the chemical equilibrium (i.e. the reaction should be unidirectional, and flux capacity is likely to explain the in vivo flux). This unidirectionality is consistent with the general notion that, in higher plants, plastidial AGPase tends to be displaced from equilibrium because of the presence of inorganic pyrophosphorylase (Tiessen et al., 2002). In the case of enolase, the enzyme activity (V_{max}) was only about 5 times higher than the total net flux from 3-PGA to PEP. In addition, estimation of the in vivo mass action ratio for the combined reactions of phosphoglycerate mutase and enolase (Table IV) suggests that the interconversion of 3-PGA and PEP is not far removed from the chemical equilibrium. We did not measure phosphoglycerate mutase, which interconverts 3-PGA and 2-PGA, but if the combined reactions phosphoglycerate mutase and enolase operate close to equilibrium, then this should be true for the enolase reaction (2-PGA → PEP) separately as well. Therefore, enolase might be working close to equilibrium and close to substrate saturation.

Identification of Metabolites Diagnostic for the Accumulation of Lipid, Protein, and Starch

The metabolic profiles of the nine entries were distinct. Principal component analysis (PCA) of the 27

Table III. *Quantitative relationship between measured enzyme capacity (V_{max}) and related net fluxes*

The V_{max}-flux ratio was derived for all seven oilseed rape entries for which enzymes were measured. Ratios were derived after scaling V_{max} and flux values to comparable units (data from Supplemental Table S6B). Enzyme abbreviations: eAGPase, ADP-Glc pyrophosphorylase; eAlaAT, Ala aminotransferase; eAldolase, Fru-1,6-bisP aldolase; eCS, citrate synthase; eF6PT-Ppi, inorganic pyrophosphate-dependent phosphofructokinase; eG6PDH, Glc-6-P dehydrogenase; eGAPDH-NAD, NAD-dependent glyceraldehyde 3-phosphate dehydrogenase; eGAPDH-NADP, NADP-dependent glyceraldehyde 3-phosphate dehydrogenase; eHK-Frc, fructokinase; eHK-Glc, glucokinase; eICDH-NAD, NAD-dependent isocitrate dehydrogenase; eICDH-NADP, NADP-dependent isocitrate dehydrogenase; ePEPC, phospho*enol*pyruvate carboxylase; ePEPCK, phospho*enol*pyruvate carboxykinase; ePKc, cytosolic pyruvate kinase; ePKp, plastidic pyruvate kinase; ePPDK, pyruvate, phosphate dikinase. Flux abbreviations: vAldo, phosphofructokinase and Fru-1,6-bisP aldolase; vAT_c, Ala/pyruvate-dependent aminotransferase activity; vCS, citrate synthase; vFM, fumarase; vG6PDH, Glc-6-P dehydrogenase; vGAPDH, glyceraldehyde 3-phosphate dehydrogenase; vHex_HPc, glucokinase/fructokinase; vICDH, isocitrate dehydrogenase; vPEPC_c, phospho*enol*pyruvate carboxylase and phospho*enol*pyruvate carboxykinase; vPGM, interconversion of 3-phosphoglycerate and phospho*enol*pyruvate; vPK, pyruvate kinase; vSt_out, flux into starch via ADP-Glc pyrophosphorylase; c, compartment-specific enzyme isoform or flux (cytosol); p, compartment-specific enzyme isoform or flux (plastid). Vertical bars indicate absolute flux value.

Enzyme	Net Flux	V_{max}-Flux Ratio	
		Average $\pm$ SD	Minimum, Maximum
eAGPase	|vSt_out|	9.0 ± 6.5	2.5, 19.4
eAlaAT	|vAT_c|	411.3 ± 107.5	287.2, 527.4
eAldolase	|vAldo_c|+|vAldo_p|	74.3 ± 13.4	55.1, 92.7
eCS	|vCS|	344.2 ± 185.7	152.3, 598.0
eEnolase	|vPGM_c| + |vPGM_p|	5.3 ± 0.8	4.1, 6.5
eF6PT-Ppi	|vAldo_c| + |vAldo_p|	28.7 ± 10.8	16.1, 46.7
eFumarase	|vFM|	280.7 ± 265.1	66.7, 753.8
eG6PDH	|vG6PDH_c| + |vG6PDH_p|	649.1 ± 1,480.2	57.5, 4005.4
eGAPDH-NAD + eGAPDH-NADP	|vGAPDH_c| + |vGAPDH_p|	51.9 ± 24.9	24.7, 97.8
eHK-Frc + eHK-Glc	|vHex_HPc|	32.7 ± 2.3	29.6, 36.1
eICDH-NAD + eICDH-NADP	|vICDH|	2,250.6 ± 3,996.7	400.2, 11,272.5
ePEPC + ePEPCK	|vPEPC_c|	219.8 ± 76.7	140.3, 357.6
ePKc + ePPDK	|vPK_c|	35.0 ± 6.0	24.7, 42.9
ePKp	|vPK_p|	15.6 ± 3.7	10.5, 21.2

experimental replicates allowed recognizing several entries as being distinct from each other (Fig. 5A). Along PC1, entries CR2186 and CR3217, both winter oilseed rape lines, separated clearly from the summer oilseed rape lines. The DGAT1 transgenic line and its genetically similar progenitor cultivar (OSR reference line) were indistinguishable in the PCA plot while differing in lipid content. At the same time, the genotype pair CR3231/CR3135 was distant on the PCA plot but almost identical in biomass composition. Overall, the PCA separated experimental replicates by entries, but the principal components PC1 and PC2 appear not to primarily separate according to variability in biomass composition. This means that our interpretation must be mindful that genotypic differences other than biomass composition are manifest in
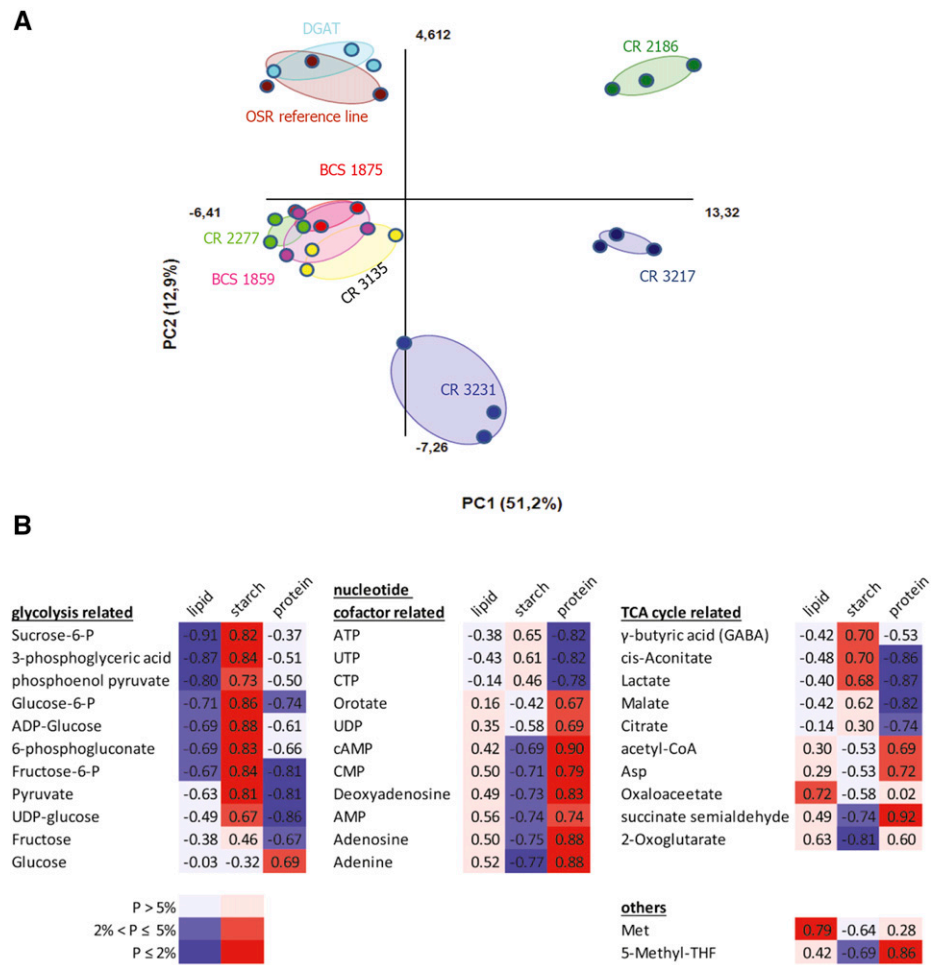
Table IV. *Estimation of in vivo molar mass-action ratios for different metabolic reactions in oilseed rape embryos*

The values of the molar mass-action ratios were calculated using the mean metabolite concentrations (Supplemental Table S5B), and the equations are given here. The respective theoretical equilibrium constant (K_{eq}) for each reaction step is shown for comparison. Values that are displaced more than 10-fold from their respective K_{eq} pinpoint irreversible reactions are indicated in boldface. Brackets indicate concentration.

Enzyme Name	Calculated Mass-Action Ratio	Theoretical K_{eq}
Suc synthase	([Frc] × [UDP-Glc])/([Suc] × [UDP]) = 0.002	**0.15**
UDP-Glc pyrophosphorylase	([Glc-1-P] × [UTP])/[PPi] × [UDP-Glc]) = 23.2	3.2
ADP-Glc pyrophosphorylase	([ADP-Glc] × [PPi])/([Glc-1-P] × [ATP]) = 0.002	**1**
Glucokinase	([Glc-6-P] × [UDP])/([Glc] × [UTP]) = 0.06	**873**
Fructokinase	([Frc-6-P] × [UDP])/([Frc] × [UTP]) = 4.6	**851**
Phosphoglucomutase	[Glc-1-P]/[Glc-6-P] = 0.34	0.05
Phosphoglucoseisomerase	[Glc-6-P]/[Frc-6-P] = 3.52	0.5
PFK	([Frc-1,6-diP] × [ADP])/([Frc-6-P] × [ATP]) = 0.035	**316**
Phosphoglycerate mutase, enolase[a]	[PEP]/[3-PGA] = 0.18	0.34
Pyruvate kinase	([Pyr] × [ATP])/([PEP] × [ADP]) = 12.3	**327,119**

[a]The common intermediate 2-phosphoglycerate (2-PGA) was not measured. Equilibrium constants of phosphoglyceromutase and enolase were combined, allowing the ratio [PEP]-[3-PGA] to be derived (Supplemental Table S5B).

Figure 5. Metabolic characterization of selected oilseed rape entries based on LC-MS quantification of metabolites in cultured embryos. Pearson correlation coefficients are shown with color coding for significance. A, Principal component analysis separating experimental replicates. B, Metabolites significantly correlated with lipid, protein, or starch ($P \leq 5\%$; Supplemental Table S6C) grouped by metabolic function and sorted by correlation to starch. TCA, Tricarboxylic acid.

A

(PC1 51,2%; PC2 12,9%) — DGAT, OSR reference line, CR 2186, BCS 1875, CR 2277, BCS 1859, CR 3135, CR 3217, CR 3231; axis values 4,612 / -6,41 / 13,32 / -7,26

B

glycolysis related	lipid	starch	protein
Sucrose-6-P	-0.91	0.82	-0.37
3-phosphoglyceric acid	-0.87	0.84	-0.51
phosphoenol pyruvate	-0.80	0.73	-0.50
Glucose-6-P	-0.71	0.86	-0.74
ADP-Glucose	-0.69	0.88	-0.61
6-phosphogluconate	-0.69	0.83	-0.66
Fructose-6-P	-0.67	0.84	-0.81
Pyruvate	-0.63	0.81	-0.81
UDP-glucose	-0.49	0.67	-0.86
Fructose	-0.38	0.46	-0.67
Glucose	-0.03	-0.32	0.69

nucleotide cofactor related	lipid	starch	protein
ATP	-0.38	0.65	-0.82
UTP	-0.43	0.61	-0.82
CTP	-0.14	0.46	-0.78
Orotate	0.16	-0.42	0.67
UDP	0.35	-0.58	0.69
cAMP	0.42	-0.69	0.90
CMP	0.50	-0.71	0.79
Deoxyadenosine	0.49	-0.73	0.83
AMP	0.56	-0.74	0.74
Adenosine	0.50	-0.75	0.88
Adenine	0.52	-0.77	0.88

TCA cycle related	lipid	starch	protein
γ-butyric acid (GABA)	-0.42	0.70	-0.53
cis-Aconitate	-0.48	0.70	-0.86
Lactate	-0.40	0.68	-0.87
Malate	-0.42	0.62	-0.82
Citrate	-0.14	0.30	-0.74
acetyl-CoA	0.30	-0.53	0.69
Asp	0.29	-0.53	0.72
Oxaloacetate	0.72	-0.58	0.02
succinate semialdehyde	0.49	-0.74	0.92
2-Oxoglutarate	0.63	-0.81	0.60

others	lipid	starch	protein
Met	0.79	-0.64	0.28
5-Methyl-THF	0.42	-0.69	0.86

P > 5%
2% < P ≤ 5%
P ≤ 2%

the metabolic profile. However, by correlation analysis (Supplemental Table S6C), we could determine that 35 of the 77 measured metabolites are significantly correlated to lipid, starch, or protein ($P \leq 5\%$; Fig. 5B). Most of these metabolites are associated with central metabolism. Suc-6-P, a number of glycolytic intermediates, as well as hexose phosphate-derived intermediates (ADP-Glc and 6-phosphogluconate) are significantly negatively correlated to lipid and mostly positively correlated to starch content (Fig. 5B). Eleven nucleotide cofactors and related metabolites are highly correlated to protein or starch and protein. In addition, 10 tricarboxylic acid cycle-related carboxylic acids and amino acids are among the correlated ones (Fig. 5B). Among the positive correlations to protein content were γ-aminobutyric acid, the signaling molecule cAMP, and several nucleotides and cofactors (Fig. 5B). Some of the metabolites identified in Figure 5B to correlate to major biomass components in the oilseed rape embryo are known as effector molecules. For example, the glycolytic intermediates PEP and 3-PGA are known to allosterically affect the enzymatic activity of ATP-dependent phosphofructokinase (PFK; Plaxton, 1996; Givan, 1999) and AGPase (Crevillén et al., 2003),

respectively. Both metabolites are negatively correlated to lipid, and their concentration ranges about 2.5-fold across the entries. We verified that the allosteric effect, formerly described to be active in the leaf, also takes place in the oilseed rape embryo, and we found the expected suppression of PFK and enhancement of AGPase activity dependent on the addition of PEP and phosphoglyceric acid, respectively (Supplemental Fig. S3, A and B). Thus, the numerous correlations identified here suggest that metabolic regulation is relevant. We also noted that trehalose-6-phosphate (an essential signaling molecule; Yadav et al., 2014) negatively correlated to Glc uptake (vuptGlucose), plastidic fatty acid synthesis/export of acetate units (vFASp), and plastidic OPPP reactions (vG6PDH_p) but did not show any significant correlation to other intermediates, including Suc (Supplemental Table S6C).

The Initial and Final Steps of Glycolysis Are Essentially Irreversible in Vivo

The quantification of metabolite levels further allowed the mass-action ratio (the ratio between the in

vivo concentration of the product and that of its substrate) to be calculated for individual enzymatic reactions. These were then compared with their respective K_{eq} (the ratio of product and reactant concentrations at which forward and reverse reaction rates are equal) to reveal how far each reaction was displaced from its chemical equilibrium (Table IV). Following Tiessen et al. (2012), we considered a reaction as irreversible when the mass-action ratio is displaced from its K_{eq} by a factor of more than 10. The outcomes indicated that both Suc cleavage mediated by Suc synthase and hexose mobilization mediated by glucokinases/fructokinases were essentially irreversible in vivo in the oilseed rape embryo (Table IV). The same applied with respect to both the following and the final glycolytic steps, catalyzed by, respectively, PFK and pyruvate kinase, as well as starch synthesis (mediated by AGPase). In contrast, various sugar phosphate conversion steps (mediated by phosphoglucomutase, phosphoglucose isomerase, and UDP-Glc pyrophosphorylase) were readily reversible. Phosphoglyceromutase and enolase were close to equilibrium as well. Overall, while one has to be mindful that these calculations did not account for any nonhomogenous subcellular distribution of metabolites, in particular the findings of irreversibility in glycolysis are consistent with the general expectation (Morandini, 2009).

Estimation of Metabolite Turnover Times

By relating the concentrations of metabolites to the relevant flux values, a calculation was made of the various turnover times (Supplemental Fig. S3, C and D). The analysis indicated that the hexose phosphates (Glc-1-P, Glc-6-P, Fru-6-P, and Fru-1,6-diP) were consumed within 10 to 50 min; turnover times were positively correlated to starch content but negatively to lipid content. The same relationships applied to glycolytic intermediates, but with shorter consumption times (PEP, 44 s; 3-PGA, 4 min; pyruvate, 7 min).

The Proteome of High-Lipid Entries Barely Differed from Low-Lipid Entries with Respect to Their Lipid, Amino Acid, or Carbohydrate Metabolism

As this work aims to decipher posttranscriptional mechanisms of metabolic control, we analyzed gene expression at the proteome level. We first generated a reference proteome map based on the genotype OSR reference line (Supplemental Table S7A). The map comprised 1,453 proteins distributed among 1,109 spots and belonging to 12 functional categories (Fig. 6A). The largest group of proteins (244 proteins, equivalent to about 17%) was involved in carbohydrate metabolism. The next most abundant category (about 13%) involved protein metabolism. Following this, a pairwise comparison was made of the proteomes of high- versus low-lipid entries (a full list of

the putatively differentially expressed proteins is given in Supplemental Table S7, B and C). The most pronounced difference was obtained between entries CR3231 and CR2277 (159 spots, 315 proteins, varying at least 1.5-fold in intensity). The DGAT1 transgenic line's profile was almost identical to that of the OSR reference line: only a single spot showed any change (decreasing by 1.5-fold). In all, 39% of the 161 proteins putatively up-regulated in the high-lipid entries were expressed specifically in the seed, most of them being storage proteins (Fig. 6A). The high-lipid entries tended to have a lower abundance of proteins involved in energy metabolism (photosynthesis and carbon fixation), barely differing from the low-lipid entries with respect to their lipid, amino acid, or carbohydrate metabolism.

Individual proteins that were consistently present in greater abundance in several of the high- or low-lipid entries were identified as potential diagnostic markers (Fig. 6, B and C). There was a consistent increase in the content of individual storage proteins in the high-lipid entries, whereas that of several enzymes involved in protein synthesis and folding was markedly reduced in at least three of the pairwise comparisons. The abundance of two tricarboxylic acid cycle enzymes (malate dehydrogenase and aconitate hydratase) was found to be increased in high-lipid lines (Fig. 6B). There was no convincing evidence for any coordinated up- or down-regulation of entire pathways, so it was concluded that the level of metabolic enzymes present was unlikely to underlie the differences in synthetic flux and, as a result, the lipid content of the embryo.

The proteomic analysis also highlighted several posttranslational modifications. In some cases, a horizontal array of spots, each containing the same protein, was generated in the two-dimensional separation (based on pI and molecular mass). A number of posttranslational modifications, notably phosphorylation and acetylation, can significantly alter a protein's pI. Malate dehydrogenase1 (the predominant mitochondrial isoform) was distributed over seven spots, all representing a product of molecular mass 33 kD (Supplemental Table S7D), with a pI ranging from 5.9 to 6.9. A decreased abundance (by 2.2- to 2.4-fold) of one of these variants (spot 490) was noted in three of the high-lipid entries. Similarly, there was an acidic shift for the glycolytic triosephosphate isomerase protein, with a greater abundance associated with spot 624 and a lower abundance associated with spots 614, 617, and 620 in the high-lipid entries. In contrast, high-pI forms of glyceraldehyde 3-phosphate dehydrogenase were more abundant in the low-lipid entries.

DISCUSSION

The rationale of this study was to characterize a representative sample of oilseed rape germplasm in a quantitative multilevel approach, with the aim of deriving an improved model for the regulation of the seed central metabolism and of identifying potentially

Figure 6. Features of high- versus low-lipid proteomes. A, Distribution of proteins showing a potentially elevated abundance in the high-lipid entries (black bars) and in the low-lipid entries (white bars) across functional categories. The full set of proteins detected in the reference proteome is shown by the gray bars. B and C, Proteins showing an elevated abundance in the high-lipid (B) and the low-lipid (C) entries. Proteins with increased abundance in at least three pairwise comparisons are listed in the table below, and the full list of proteins is given in Supplemental Table S7.
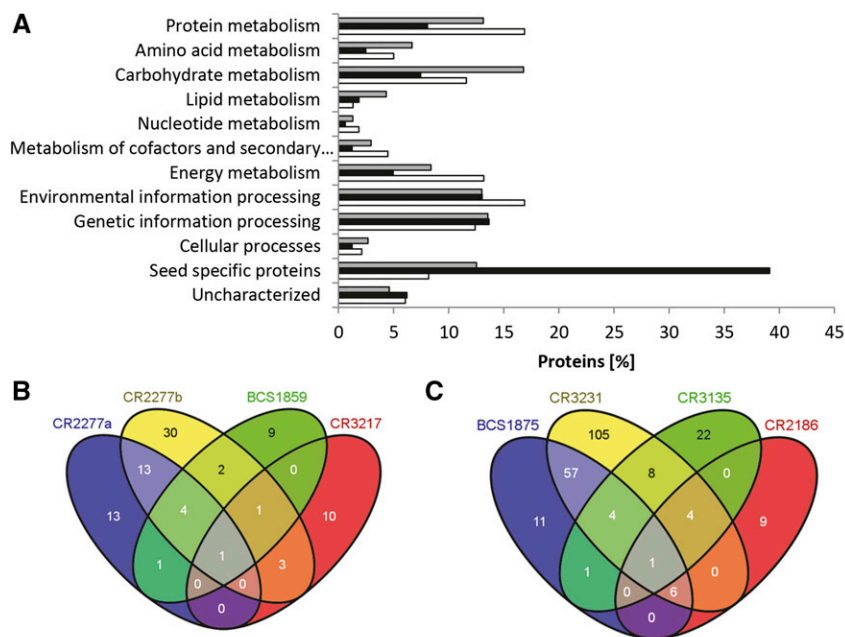
Accession	Name	Categorie	Function	A	B	C	D
Proteins with increased abundance in high oil lines							
P33525	Cruciferin CRU1	Seed specific proteins	Storage	x	x	x	x
P11090	Cruciferin CRUA	Seed specific proteins	Storage	x	x	x	
P33522	Cruciferin CRU4	Seed specific proteins	Storage	x	x	x	
P09893	Napin embryo-specific	Seed specific proteins	Storage	x	x	x	
P33524	Cruciferin BnC2	Seed specific proteins	Storage	x	x	x	
O04005	1-Cys peroxiredoxin PER1	Seed specific proteins	Seed maturation		x	x	x
Proteins with increased abundance in low oil lines							
Q42560	Aconitate hydratase 1	Carbohydrate metabolism	TCA cycle	x	x	x	
At1g53240	Malate dehydrogenase 1, mitochondrial	Carbohydrate metabolism	TCA cycle	x	x		x
AT1G66410	CAM4, calmodulin 4	Env. information processing	Signaling	x	x	x	
AT3G53990	Adenine nucleotide alpha hydrolase	Env. information processing	Stress response	x	x	x	
AT1G12270	Hop1 stress-inducible protein	Env. information processing	Stress response	x	x		x
AT5G57290	60S acidic ribosomal protein family	Genetic information processing	Ribosome	x	x	x	
AT3G11710	ATKRS-1 lysyl-tRNA synthetase 1	Genetic information processing	Translation	x	x		x
AT4G37910	mitochondrial heat shock protein 70-1	Protein metabolism	Protein folding		x	x	x
AT3G12740	Heat shock cognate 70 kDa protein 4	Protein metabolism	Protein folding		x	x	x
Q03685	Luminal-binding protein 5	Protein metabolism	Protein folding		x	x	x
AT3G25530	70 kDa peptidyl-prolyl isomerase	Protein metabolism	Protein folding		x	x	x
P49118	Luminal-binding protein	Protein metabolism	Protein folding	x	x		x
AT5G28540	BIP1 heat shock protein 70	Protein metabolism	Protein folding	x	x		x
O04005	1-Cys peroxiredoxin	Seed specific proteins	Seed maturation	x	x		x
P33525	Cruciferin CRU1	Seed specific proteins	Storage	x	x	x	x

Genotype comparison in column A: CR2277 vs. BCS1875; B: CR2277 vs. CR3231; C: BCS1859 vs. CR3135; D: CR3217 vs. CR2186.

diagnostic markers for the composition of the embryo. We performed a detailed biochemical analysis of nine oilseed rape lines, studying metabolite levels, enzyme activities, fluxes, and proteomes. Since this study is based on an in vitro system to mimic seed development, one has to keep in mind that the cultured embryos are not fully equivalent to a seed developing in planta (Borisjuk et al., 2013a). Transfer of conclusions from in vitro to in planta will need additional experimental verification. Nevertheless, the observed lipid/starch tradeoff along with numerous correlations allowed drawing unambiguous conclusions about which pathways/metabolites/enzymes in intermediary metabolism are relevant for carbon partitioning. The conclusions and models will be

both a rich source of data and of considerable interest to those studying the regulation of plant intermediary metabolism.

Flux Distribution Measured across Oilseed Rape Genotype Entries Allows the Inference of Regulation in Central Metabolism

We determined the flux distribution in central metabolism of developing embryos for nine oilseed rape genotype entries (Fig. 4; Supplemental Table S3G). Among genotypes, the flux distribution is mostly consistent with previously published results (Schwender et al., 2003, 2004, 2006). For example, the conversion of

substrate Glc via glycolysis into lipids is a preeminent feature of carbon flow shown in Figure 4. Besides glycolysis, about 50% of the conversion of sugars into lipids takes place by the Rubisco shunt (Schwender et al., 2004; Table II). In this and in former studies, flux through the tricarboxylic acid cycle is consistent with the tricarboxylic acid cycle being used only to a limited extent for catabolism/energy cofactor generation (Schwender et al., 2006). Among genotypes on average, 69% of plastidic pyruvate entering fatty acid synthesis is derived via plastidic pyruvate kinase (Table II). While these common features of flux distribution in central metabolism define a common pattern of pathway usage in cultured oilseed rape embryos, this study associates genotypic variability in biomass composition with changes in flux distributions. This means that our flux results now allow the direct inference of metabolic regulation, which is extended by metabolome, enzyme, and proteome data measured in parallel.

OPPP Flux Might Be Important But of Minor Contribution to Fatty Acid Biosynthesis

Relative to starch or protein synthesis, the formation of lipid has very high demands in the reducing cofactors NADH and NADPH (Schwender and Hay, 2012). Flux through the plastidic OPPP (vG6PDHp) was positively correlated with plastidial fatty acid synthesis ($R = 0.78$), indicating its importance for lipid synthesis in providing reductant. However, by far, not all of the NADPH required for fatty acid synthesis can be derived from plastidial OPPP. If NADPH production is inferred by OPPP flux (two NADPHs per molecule of Glc-6-P oxidized) and expressed relative to NADPH consumption based on fatty acid biosynthetic flux (vFASp), only between 0% and 9% of the NADPH demand for de novo fatty acid synthesis is supplied by plastidic OPPP (Table II). Even when considering the combined cytosolic and plastidic OPPP fluxes to derive the NADPH balance for plastidic de novo fatty acid synthesis, the total OPPP flux meets on average 36%, maximal 62% of the NADPH demand (Table II). This finding parallels former flux studies with oilseed rape 'Reston' embryos under the same conditions, where the maximal 38% of NADPH needed for fatty acid synthesis was estimated to be delivered by cytosolic and plastidic OPPP (Schwender et al., 2003). Since the embryo cultures are grown photoheterotrophically, the remainder of the NADPH required for fatty acid synthesis can be assumed to be contributed by photosynthetic activity (Borisjuk et al., 2013a). For nonphotosynthetic lipogenesis, the OPPP had to produce all of the reductant. Accordingly, for sunflower and maize (*Zea mays*) developing embryos, it was estimated that OPPP produces more than 70% of the NADPH required for fatty acid synthesis (O'Grady et al., 2012). However, besides the literature-postulated role of OPPP to be the predominant source of reductant

for biosynthetic processes like lipid synthesis or nitrogen assimilation in nonphotosynthetic tissues, in silico constraint-based analysis of central metabolism in oilseed rape developing seeds allows the efficient conversion of sugars into fatty acids and lipids in the dark without any contribution of OPPP (Hay and Schwender, 2011).

Provision of Precursors for Cytosolic Elongation of Fatty Acids

In oilseed rape seeds, very-long-chain fatty acids are abundant in seed oil and formed by cytosolic extension of C18 chains, which requires cytosolic acetyl-CoA being produced via ATP:citrate lyase (Cassagne et al., 1994; Schwender and Ohlrogge, 2002). In all modern oilseed rape low-erucic acid accessions, the reduction in cytosolic fatty acid elongation is considered to be due to the loss of function in a gene homolog to Arabidopsis FATTY ACID ELONGASE1 (Wu et al., 2008; Wang et al., 2010); that is, the elongation process itself seems to be disrupted, not the precursor supply. Our study includes low- and high-erucic acid oilseed rape cultivars. For six genotypes, the in vitro cultured embryos were almost completely devoid of very-long-chain fatty acids, while in lines CR3231, CR2277, and CR3217, the percentage of fatty acids more than 18 carbons in length was 40%, 48%, and 52%, respectively (Supplemental Table S2). This variability in oil composition was reflected among the genotypes in the flux distribution, and flux regulation is recognized based on flux correlations (Table I). Within the spectrum of the studied genotypes, the fatty acid elongation flux (vFAEc; Fig. 4) changed dramatically (about 50-fold). Up-regulation of cytosolic fatty acid elongation is achieved by concerted up- and down-regulation at the citrate node (Fig. 4), which can be derived from the flux correlations listed in Table I: flux of pyruvate from cytosol to the mitochondria (vPyr_cm) and through mitochondrial pyruvate dehydrogenase, citrate synthase (vCS), and ATP:citrate lyase is positively correlated to cytosolic fatty acid elongation (Table I); at the same time, flux through aconitase/isocitrate dehydrogenase (vICDH), which competes for citrate with the cytosolic elongation, is negatively correlated to cytosolic fatty acid elongation. This means that, as the cytosolic elongation increases, more of the precursor citrate is produced by ATP:citrate lyase and less citrate is converted to 2-ketoglutarate. It should be noted that the up-regulation of cytosolic fatty acid elongation might be possible by an entirely different means of citrate provision. Gln is an abundant and much-used carbon source in our in vitro system and could be converted to citrate (Fig. 4). This has been observed in mammalian cells, where citrate is the general precursor of fatty acid synthesis. It has been reported for mammalian cell cultures that the medium substrate Gln can be utilized as a main carbon source for fatty acid synthesis, via a reaction sequence that includes the

Schwender et al.

conversion of Glu into 2-ketoglutarate, which is then further converted into citrate via parts of the citrate cycle operating in reverse (Yoo et al., 2008). The indicated pathway would be possible in cultured oilseed rape embryos in particular, since we have shown before that in cultured oilseed rape embryos, the isocitrate dehydrogenase step is reversible (Schwender et al., 2006), and thus a reductive carboxylation passage through the citrate cycle might be possible. The correlated analysis in our plant system now indicates that provision of citrate via the passage of pyruvate through citrate synthase and ATP:citrate lyase seems to be preferred.

Moreover, our analysis suggests that the provision of precursor (acetyl-CoA) for cytosolic fatty acid elongation might be largely controlled by the biosynthetic demand. Despite the marked variability in flux related to cytosolic fatty acid elongation, we did not detect correlated changes in enzyme activities. High enzyme activities (V_{max}) relative to flux were found for citrate synthase and isocitrate dehydrogenase (Table III), suggesting that flexible adjustments of the tricarboxylic acid cycle to different biosynthetic demands by cytosolic fatty acid elongation are not based on transcriptional regulation (i.e. possibly by metabolic regulation). When cultured with organic or inorganic nitrogen supplies, clear differences in flux distribution around the tricarboxylic acid cycle were observed, while corresponding changes in relevant enzyme activities could not be detected. This finding is in line with former in vitro studies with oilseed rape developing embryos (Junker et al., 2007).

Multifaceted Control of Plastidic Fatty Acid Synthesis

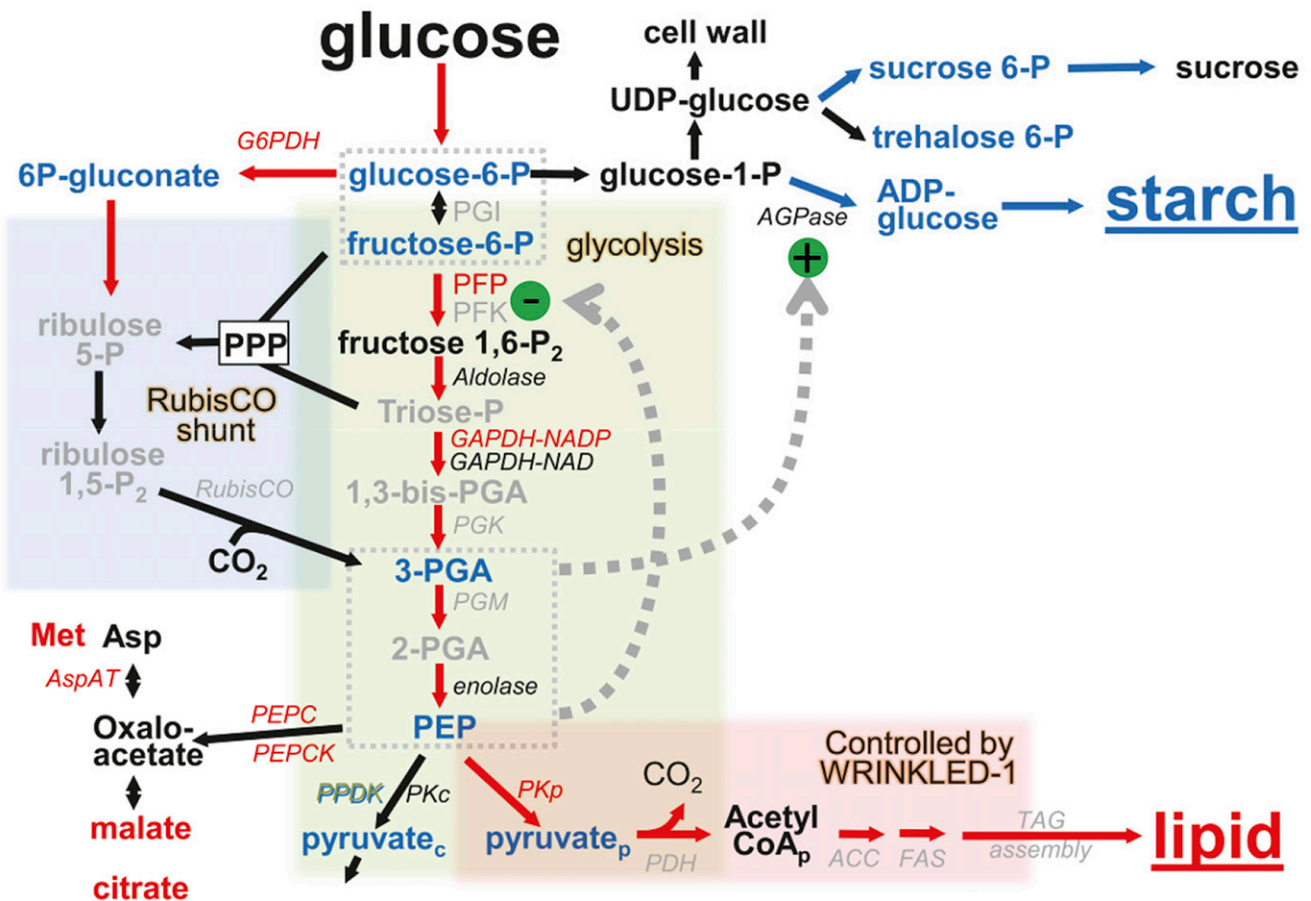The comparison of the nine oilseed rape entries also allows deepened insight into the control of carbon flux

Figure 7. Simplified conceptual model for the central metabolism of oilseed rape and the regulation of carbon partitioning. The network shown represents the most relevant pathways and includes all measured metabolites with strong correlation to flux into fatty acid synthesis or starch ($P < 2\%$). Nonmeasured metabolites are added to complete pathways and are shown in gray. All color-coded fluxes, enzymes, and metabolites have opposite signs in correlation coefficients for lipid and starch, respectively. Red color indicates positive correlation to lipid and negative correlation to starch, being at least in one case highly significant ($P < 2\%$). ACC, Acetyl-coenzyme A carboxylase; FAS, fatty acid synthesis; G6PDH, Glc-6-P dehydrogenase; GAPDH, glyceraldehyde 3-phosphate dehydrogenase; HK-Glc, hexokinase; PDH, pyruvate dehydrogenase; PEPCK, phospho*enol*pyruvate carboxykinase; PGI, phosphoglucose isomerase; PGK, phosphoglycerate kinase; PGM, phosphoglycerate mutase; PPDK, pyrophosphate:pyruvate dikinase; PPP, pentose phosphate pathway.

into plastidial fatty acid synthesis. Across the entries, with increase in lipid content, the combined cytosolic and plastidic fluxes for the conversion of 3-PGA to PEP increases by about 30%, while the steady-state levels of glycolysis intermediates were negatively correlated to lipid (Fig. 5B) and hence decreased with increasing glycolysis flux. In particular, 3-PGA and PEP decreased about 2.5-fold with increasing flux into lipids. This is at first counterintuitive if we consider that a higher conversion rate of any enzyme step in an up-regulated pathway should require higher substrate concentration. To explain how glycolytic flux might be regulated in coordination with fatty acid and lipid synthesis and in an attempt to integrate our findings and the literature on plant central metabolism, we derived a simplified scheme of intermediary metabolism and its regulation (Fig. 7). First, we consider Glc-6-P and Fru-6-P as a combined metabolic pool (Fig. 7), since the interconversion of these two by phosphoglucoseisomerase was determined to be close to equilibrium (Table IV). This combined hexose phosphate pool can be understood as a central metabolic branch point, with effluxes into starch synthesis, cell wall synthesis, OPPP, the Rubisco shunt (Schwender et al., 2004), and glycolysis (Fig. 7). 3-PGA is derived from both glycolysis and the Rubisco shunt, both sharing the sequential steps of PFK and aldolase (Fig. 7). Enzyme activity of PFP was found to be positively correlated to lipid (Supplemental Table S6C), suggesting that PFK might be a control step for entry into glycolysis and the Rubisco shunt. Although our set of measured enzymes did not include ATP-dependent PFK, PFK isoforms are known to be highly expressed in oilseed rape developing seeds (Troncoso-Ponce et al., 2011). PFK could be a metabolic control point as well, since it seems to be far removed from the chemical equilibrium (Table IV).

Assuming the phosphorylation of Fru-6-P to Fru-1,6-bisP to be a committed step and control point (Plaxton, 2004), the classical crossover theorem would suggest that increased glycolytic flux is accompanied by a decrease in substrate (hexose phosphates) and an increase in product (Fru-1,6-bisP) and downstream glycolytic intermediates. This kind of observation has been made in plants (Faiz-Ur-Rahman et al., 1974). While the decrease in hexose phosphates was indeed observed, we could not observe a significant change in Fru-1,6-bisP levels, and the levels of glycolytic intermediates farther downstream (PEP and 3-PGA) did not increase but decreased instead. Therefore, the data do not clearly support dominant control of glycolysis at the PFK step. Given that PFP and PFK are known to be strongly affected by various allosteric effectors (Turner and Plaxton, 2003; Plaxton and Podestá, 2006), allosteric control might dominate the control of enzyme abundance over pathway flux. Looking farther downstream in glycolysis, our analysis showed that PKp enzyme activity is positively correlated with lipid accumulation (Fig. 7). PEP, a substrate of PKp, was negatively correlated to lipid (Fig. 5B), and across the oilseed rape entries, its measured concentration ranges substantially by about 2.5-fold. Taken together, this suggests the dominance of an allosteric feedback-control mechanism of glycolysis that has been widely described and analyzed in plants (Hatzfeld and Stitt, 1991; Plaxton, 1996; Givan, 1999; Plaxton and Podestá, 2006); the notion is that the control of glycolytic flux is exerted via a feedback inhibition of ATP-dependent PFK, mainly via PEP (Plaxton, 1996). Plant PFK is strongly inhibited by PEP (Plaxton and Podestá, 2006), and cytosolic and plastidic PFK isoforms are expressed in oilseed rape developing seeds (Troncoso-Ponce et al., 2011). While not measured in our study across the nine entries, we confirmed the inhibition of the enzyme activity by PEP in crude extracts of developing embryos (Supplemental Fig. S3, A and B). The PFP measured in our study has been reported to be inhibited by PEP as well. In particular, PEP was reported to attenuate the potent activation of PFP via Fru-2,6-bisP (Theodorou and Plaxton, 1996; Theodorou and Kruger, 2001). Moreover, PEP was shown to strongly inhibit Fru-6-P 2-kinase (i.e. the synthesis of Fru-2,6-bisP; Villadsen and Nielsen, 2001). We hypothesize that the increase in PKp enzyme level, as observed in oilseed rape developing seeds among genotypes, has a strong impact on glycolytic flux by decreasing the level of its substrate, PEP, which in turn allosterically relieves the inhibition of one or both of the PFK activities (Fig. 7). In agreement with this regulation scheme, it has been well established that, in developing Arabidopsis and oilseed rape seeds, PKp is under the control of WRINKLED1, an important transcriptional regulator of oil accumulation in maturing seeds (Cernac and Benning, 2004; Cernac et al., 2006; Baud et al., 2009; Maeo et al., 2009).

Control of Carbon Partitioning between Lipid and Starch

In the context of the observed lipid/starch tradeoff, this concept of feedback control can be extended to starch synthesis (Fig. 7). Starch is synthesized in plastids from ADP-Glc, which is positively correlated to starch content (Fig. 5B). ADP-Glc is formed by AGPase, an enzyme representing an important control step in starch synthesis (Sweetlove et al., 1999) and allosterically affected by the 3-PGA-inorganic phosphate ratio (Preiss 1988; Crevillén et al., 2003). The allosteric stimulation by high phosphoglyceric acid/inorganic phosphate was also evident in the oilseed rape embryo (Supplemental Fig. S3), which led us to the following hypothesis on the regulation of carbon partitioning in oilseeds: rising concentrations of the two glycolytic intermediates PEP and 3-PGA promote starch synthesis but repress glycolytic flux, while falling concentrations (e.g. due to high rates of fatty acid synthesis) shift carbon partitioning toward glycolysis (Fig. 7). Notably, the concentrations of PEP and 3-PGA are highly correlated ($R = 0.96$), and the ratio [3-PGA]-[PEP] suggests that both are close to equilibrium (Table IV), supporting the notion that the feedback controls of starch and lipid synthesis are coordinated.

Our findings here bear out what seems well-described regulatory feedback mechanisms in plant glycolysis and starch synthesis, but in previously unprecedented multilevel detail and specifically related to carbon partitioning in oilseeds. The feedback-control mechanism makes sense in the context of the master regulator WRINKLED1 being established to have PKp and several of its downstream reactions as main targets (Baud et al., 2009; Maeo et al., 2009). The proposed coordinated bottom-up control of glycolysis and starch synthesis is further supported by the study of Arabidopsis mutants carrying defective PKp subunits (Andre et al., 2007; Baud et al., 2007). Accordingly, developing mutant seeds accumulate much more starch than do wild-type ones. At the same time, increased PEP and pyruvate levels were reported for the mutant, which is consistent with the idea of swelling of PEP levels in response to a reduction in PKp (Andre et al., 2007). Similar to PKp mutations, in PKc-deficient tobacco (*Nicotiana tabacum*) plants, the level of PEP in leaves was found to be significantly increased as compared with the wild type (Gottlob-McHugh et al., 1992).

Complexity of Subcellular Compartmentation

Our scheme (Fig. 7) of metabolic control of lipid/starch partitioning in oilseeds has been established with only limited consideration of cellular compartmentation. Application of nonaqueous fractionation protocols would be needed to experimentally resolve metabolite compartmentation (Tiessen et al., 2012), but this technically challenging approach was not applicable. While we could not determine the distribution of metabolites among different subcellular compartments, for the interpretation of metabolite data in our study, it is of interest to know which of the measured metabolites are likely to be found predominantly in the metabolically highly active compartments (i.e. the cytosol, plastid stroma, and other smaller compartments). Nonaqueous fractionation and metabolite profiling in different plant tissues suggest that phosphorylated intermediates and a number of other intermediates measured in this study tend to be found mainly in cytosol and plastid stroma, while metabolites such as Suc, Glc, several amino acids, or organic acids such as citrate and malate are often found at significant or at highest levels in the vacuole (Farré et al., 2001; Tiessen et al., 2002, 2012; Szecowka et al., 2013). Therefore, for such metabolites that tend to be vacuole localized, measured changes in tissue levels might reflect only variation in the vacuole levels. However, for metabolites that are distributed across metabolic highly active compartments, a change of total concentration likely reflects changes in the state of the metabolic network.

Our conclusion on PFK being mainly controlled allosterically gains further support from transgenic studies. It has been shown that transgenic overexpression of ATP-PFK in plants is not effective in stimulating glycolysis, and it was suggested that this is likely due to changes in allosteric effectors of the enzyme in overexpression lines (Stitt and Sonnewald, 1995; Thomas et al., 1997a, 1997b). Furthermore, with regard to the subcellular organization of the feedback control, flux analysis implies the importance of the cytosolic fructokinase step (Fig. 4). The dominance of cytosolic over plastidial glycolysis flux (Fig. 4) was common to all entries and agrees with the reported predominant expression of cytosolic isoforms of upper glycolysis enzymes in developing oilseed rape seeds (Troncoso-Ponce et al., 2011). PEP is expected to cross into the plastids at the PEP/phosphate translocator (Fischer et al., 1997). If this transporter is highly abundant and in vivo reversible, the modulation of plastidial PEP levels by PKp can be thought to be propagated across the chloroplast envelope so that the feedback control can take place in the cytosol. Accordingly, the PEP/phosphate translocator has been ascribed an important role in lipid synthesis (Ruuska et al., 2002; Kubis et al., 2004), and its overexpression in tobacco seeds has been demonstrated to promote lipid accumulation (Fuchs et al., 2013).

Combining flux and metabolite data, we estimated how fast specific intermediates are being turned over. Turnover times can be related to the response time of metabolism to environmental perturbations. In photosynthetic active leaf tissues, turnover times for most intermediates of the Calvin-Benson-Bassham cycle are close to 10 s or faster (Arrivault et al., 2009; Hasunuma et al., 2010), which reflects the potential for quick responses to changes in the light environment. Based on our flux and metabolite data, we estimated longer turnover times in the range of 1 min to 1 h, which might be indicative of the relatively stable conditions within a developing seed.

Metabolic versus Transcriptional Control

A recent study (Schwender et al., 2014) investigated the extent to which metabolic flux in the central metabolism of oilseed rape is reflected in the transcriptome. With a few exceptions, differential activity in the major pathways (glycolysis, tricarboxylic acid cycle, amino acid, and fatty acid synthesis) was not reflected in the contrasting abundances of the relevant transcripts. Here, we investigated gene expression at the proteome level. The major difference between the high- and low-lipid entries was accounted for mainly by storage proteins and protein metabolism. There was no evidence for any coordinated up/down-regulation of the central metabolic pathways, and entry-to-entry variation only concerned two metabolic enzymes. The major discordance between metabolic flux, V_{max}, and enzyme abundance suggests that fluxes in seed central metabolism were not significantly regulated at the level of transcription/translation but rather at the posttranslational level. Transcriptional control is particularly improbable where V_{max} values are orders of

magnitude greater than the steady-state flux, which in the oilseed rape embryo was clearly the case for the tricarboxylic acid cycle enzymes (Table III). Metabolic flux control exerted via changes in enzyme concentration is costly (Piques et al., 2009) and relatively slow. In contrast, posttranslational flux control may allow the seed to be more flexible in adjusting fluxes to reflect changes in substrate availability (e.g. being much higher during the daylight hours than during the night). Transcriptional control in the seeds is associated with stage-specific metabolic capacities (Belmonte et al., 2013), while flux in the central metabolism seems rather regulated by substrate availability, allosteric control, and/or posttranslational modification. The latter is supported by the observation that most glycolytic and tricarboxylic acid cycle enzymes present in the seed are phosphorylated and/or acetylated (Finkemeier et al., 2011; Meyer et al., 2012). Some enzyme protein modifications were also noted in our materials. Similar conclusions on flux control in central metabolism were recently drawn for microorganisms. For *Bacillus subtilis* grown under a variety of physiological conditions, changes in enzyme concentrations were insufficient to explain the observed changes in flux in central metabolism (Chubukov et al., 2013).

Limitations of the Inference of Regulation

Our suggested posttranscriptional regulatory mechanism for the control of glycolysis and carbon partitioning is based on correlative analysis across flux, metabolite, and enzyme data but still requires further experimental verification. Due to the targeted approach in flux, metabolite, and enzyme measurements, our multilevel analysis might not detect other relevant metabolic and genetic controls. For example, the lipid assembly network certainly is important for flux control in oilseeds (Tang et al., 2012), but its components are less covered in our approach (which focuses on central metabolic pathways). Also, across the entries, genotypic differences unrelated to carbon partitioning are likely to be present and could manifest in variability in the measurements that mask correlations relevant to carbon partitioning. Furthermore, of the many highly significant correlations in our data set, some might still be relevant to carbon partitioning but are currently not integrated into our conceptual model. For example, both the cytosolic flux and enzyme activity of glyceraldehyde 3-phosphate dehydrogenase were significantly correlated to lipid accumulation in oilseed rape embryos. A recent study suggests the significance of this glycolytic step for oil accumulation in developing Arabidopsis seeds (Guo et al., 2014). Also, a number of metabolites have been shown to be highly correlated with the various embryo biomass constituents (Fig. 5B), and no known regulatory function has been associated with many of them to date. These include Suc-6-P, a precursor of Suc. Its fairly low concentration (pmol mg^{-1} dry weight range) in the oilseed rape embryo corresponds to

that typically measured for signaling compounds. Defining the role of such intermediates requires a large-scale and systematic analysis of metabolite-protein interactions (Li et al., 2010). We further noticed that cAMP was significantly correlated with starch and protein storage (Fig. 5B). cAMP is well established as a secondary messenger in both microorganisms and animals and has been shown to be involved in metabolic flux control (You et al., 2013). Several plant ion channels and thioesterases are known to possess cyclic nucleotide-binding domains, associated with a wide range of physiological responses (Bridges et al., 2005). The function of cAMP in the plant cell is still unclear, but the strong correlation of its accumulation with protein storage activity suggests a hitherto unknown mechanism of metabolic flux control. Our study supports earlier findings showing that levels of trehalose-6-phosphate correlate to sugar availability (Yadav et al., 2014), but we did not observe the generally assumed link to the rate of starch synthesis (Lunn et al., 2006). Instead, low trehalose-6-phosphate levels coincided with maximum rates of plastidic OPPP and fatty acid synthesis reactions. While the underlying mechanisms remain elusive, this adds novel physiological functions to this essential signaling molecule. In case metabolite markers identified here are also valid for field-grown seed material, their diagnostic for the accumulation of lipid, protein, and starch might be used in line selection and future breeding programs (Feher et al., 2014).

Relevance of in Vitro Results for in Planta Seed Characteristics

Since this study is based on an in vitro system, one has to keep in mind that embryos growing in culture are not fully equivalent to those developing in planta (Borisjuk et al., 2013a). Yet, we deem the choice of our experimental system to be useful for several reasons. In multiple ^{13}C-based MFA studies, our in vitro embryo culture system has proven to allow well-resolved measurements of flux distribution in central metabolism (Schwender and Ohlrogge, 2002; Schwender et al., 2003, 2004, 2006; Goffman et al., 2005; Junker et al., 2007), which is currently not achievable with a similar experimental system in planta. One further possible limitation of the in vitro system is related to the role of potential oxygen limitation during seed development. While there are no indications that in vitro-grown embryos of oilseed rape lack oxygen (Goffman et al., 2005), contrasting data have been reported for in planta developing embryos (Vigeolas et al., 2003). Under relatively low ambient light levels, reduced oxygen tension can have a strong impact on the energy state in developing oilseed rape seeds, change metabolic fluxes, and impact oil content. Yet, it has been shown that under ambient light intensities comparable to field conditions, the photosynthetic oxygen evolution in green photosynthetic seeds may be sufficient to prevent hypoxia (Ruuska et al., 2002; Goffman et al., 2005; Borisjuk et al., 2013a).

The interpretation of the lipid/starch tradeoff likewise needs to consider the specifics of in vitro versus in planta growth. Embryo growth in vitro (i.e. under unrestricted [steady-state] assimilate supply) is associated with a continuous accumulation of starch. In planta, starch accumulation occurs during early developmental stages but stops once embryo growth (enlargement) ceases (Borisjuk et al., 2013a). Starch becomes completely degraded, prompting questions about its physiological relevance (da Silva et al., 1997; Baud et al., 2002; Andriotis et al., 2010). Transitory starch accumulation was suggested to be required for the seed to reach final oil content and thus was important for establishing the seed as a sink organ. However, embryo-specific suppression of AGPase in oilseed rape only delayed oil accumulation during seed development, while mature seeds had wild-type seed oil content (Vigeolas et al., 2004). The genotypic lipid/starch tradeoff observed in this study is not necessarily a predictor for genotype-specific seed oil content in planta. Yet, in elucidating the allosteric regulation, our study suggests that, during seed development in planta, the occurrence of transitory starch during the early phase of embryo development might be understood as a side effect of a not fully developed biosynthetic demand for fatty acid synthesis during early seed filling (but not as an event physiologically required to achieve seed filling). Later on, the increase in biosynthetic demand for fatty acid synthesis (in particular pyruvate kinase) might cause the shift in flux distribution at the Glc-6-P node toward glycolysis and fatty acid synthesis, which simultaneously diminishes flux into starch (and eventually leads to starch degradation once embryo growth ceases; Borisjuk et al., 2013a).

CONCLUSION

The application of an integrated multilevel quantitative approach has led to a model for metabolic regulation in the seed central metabolism of an important oil crop. These findings might be the basis for improved strategies for the metabolic engineering of seed composition. The analysis has shown that the V_{max} of glycolytic, tricarboxylic acid cycle, and other pathway enzymes seldom corresponded to either embryo composition or intracellular flux, while the levels of several metabolites (substrates, products, and effectors) involved in the regulation of enzyme activity were quite variable. Our observations lend support to the often suggested notion that, particularly in central metabolism, (1) increase in flux does not necessarily require shifts in enzyme protein abundance affected by transcriptional/translational control, (2) the flux capacity (enzyme concentration) is mostly in excess, and therefore (3) allosteric control is likely to be dominant in the regulation of central metabolism. In our case, more experimental evidence is needed to more firmly establish the importance of the described feedback mechanisms by well-controlled perturbation experiments.

MATERIALS AND METHODS

Plant Growth and Procedure for in Vitro Screening

Plants of oilseed rape (Brassica napus) were grown in a phytochamber at 18°C with 16 h of light (400 μmol quanta m^{-2} s^{-1}) and a relative air humidity of 60%. At the time of flowering, plants were tagged for the determination of developmental stages. At 20 d after flowering, intact embryos were isolated and then kept in liquid culture for 10 d under photoheterotrophy (50 μmol quanta m^{-2} s^{-1}) at 20°C with organic nitrogen sources according to previously established protocols (Schwender et al., 2006). Embryos from each genotype were grown in three independent batches. After 10 d of culture, embryos were weighed, freeze dried, and weighed again for the determination of fresh and dry weights. Embryo material was pulverized and used for the quantification of total lipid content (using time-domain NMR as described by Fuchs et al. [2013]), fatty acid composition (using gas chromatography as described by Borisjuk et al. [2013a]), and total protein content (measured as total nitrogen × 5.64 using elemental analysis as described by Borisjuk et al. [2013a]). This in vitro system has been used in former studies to describe flux distribution and pathway usage in central metabolism, which demonstrated that major aspects of in planta seed metabolism can be mimicked in vitro (Schwender et al., 2003, 2004, 2006; Schwender, 2008). The oilseed rape accessions used in this study can be derived from the IPK gene bank (http://www.ipk-gatersleben.de/en/resources/genebank-information-system/).

In Vitro Culture of Embryos and ^{13}C-Based MFA of Selected Genotypes

Embryos of nine genotypes (OSR reference line, DGAT, BCS1875, CR2277, CR3231, CR2186, CR3217, CR3135, and BCS1859) were dissected aseptically about 20 d after flowering and grown in a liquid medium at 20°C under continuous light (50 μmol m^{-2} s^{-1}). Cultures were kept in tissue culture flasks with vented seal caps (CytoOne T75; CC7682-4875; USAScientific) containing 13 mL of liquid medium and four embryos per flask. The liquid growth medium contained 20% (w/v) polyethylene glycol 4000 and the carbon and nitrogen sources Glc (120 mM), Gln (35 mM), and Ala (10 mM). Labeling experiments contained unlabeled Glc (96 mM) as well as [U-^{13}C$_6$]Glc (12 mM) and [1,2-^{13}C$_2$]Glc (12 mM). Inorganic nutrients were used similarly to Schwender et al. (2003): CaCl$_2$ (5.99 mM), MgSO4 (1.5 mM), KCl (4.69 mM), KH$_2$PO$_4$ (1.25 mM), Na$_2$EDTA (14.9 mg L^{-1}), FeSO$_4$·7H2O (11.1 mg L^{-1}), H$_3$BO$_3$ (12.4 mg L^{-1}), MnSO$_4$H$_2$O (33.6 mg L^{-1}), ZnSO$_4$·7H$_2$O (21 mg L^{-1}), potassium iodide (1.66 mg L^{-1}), Na$_2$MoO$_4$·2H$_2$O (0.5 mg L^{-1}), CuSO$_4$·5H$_2$O (0.05 mg L^{-1}), CoCl$_2$·6H$_2$O (0.05 mg L^{-1}), nicotinic acid (5 mg L^{-1}), pyridoxine hydrochloride (0.5 mg L^{-1}), thiamine hydrochloride (0.5 mg L^{-1}), and folic acid (0.5 mg L^{-1}). pH was adjusted to 5.8 using KOH. Growth medium was sterilized by 0.22-mm sterile vacuum filter units (Stericup; Millipore). After 10 d of culture, embryos were harvested, rapidly rinsed with NaCl solution (0.33 M), and after determination of fresh weight, embryos were frozen in liquid nitrogen and stored in −80°C. Experiments using unlabeled substrates were done in three replicates to determine growth kinetics and biomass composition. Experiments using labeled substrates were done in four replicates to determine metabolic fluxes. Flux analysis was performed using the 13CFLUX2 toolbox (Weitzel et al., 2013) as described in Supplemental Methods S1. The ^{13}C-based MFA model (Hay et al., 2014) is defined by 14 free net fluxes as well as 21 biomass effluxes (Supplemental Table S3B), which are derived from the biomass compositions of the different genotypes (Supplemental Table S2) and growth rates (Supplemental Table S3D). Uptake fluxes of Glc, Ala, and Gln, as well as the net efflux of CO_2 into the environment, however, depend on isotope tracer-based flux parameter fitting like the steady-state fluxes in central metabolism. Therefore, an initial validation of the flux parameter fitting results can be made by assessing the carbon conversion efficiency, given by:

$$((\text{total carbon uptake flux}) - (\text{carbon efflux}))/(\text{total carbon uptake flux}),$$

based on uptake fluxes of Glc, Gln, and Ala and CO_2 net efflux. The resulting carbon conversion efficiency values ranged genotype specifically between 79% and 86% (Table II), which is in good agreement with the value of 86% determined before by experimental carbon mass balance of medium substrates, CO_2 emission, and biomass formation for oilseed rape embryos cultured under similar photoheterotrophic conditions (Goffman et al., 2005).

Statistical evaluation of flux values was done by a Monte Carlo approach, based on repeated random resampling of the MS data and flux measurements according to the measurement SD values and redetermination of fluxes by

random-start optimization. For each genotype, the resampling of measurements was done 10 times, selecting the best fit for 20 random-start opimizations. For the OSR reference line, the random sampling was also repeated 50 times, which resulted in similar estimates for the SD values. Based on the SD values of fluxes so obtained (Supplemental Table S3G), we assessed the statistical quality of the fluxes as follows. For a given flux, the SD had to be smaller than 10% of the largest absolute value across all net fluxes and genotypes. For a given flux, this criterion had to hold across all genotypes. Accordingly, seven fluxes (vGAPDH_c, vGAPDH_p, vGPT, vPGM_c, vPGM_p, vPPT, and vTPT) were found to be not well determined. These constitute parts of the two parallel sections of glycolysis in the cytosol and the plastid compartment.

Metabolite Extraction and Analysis

Metabolite analysis was done using LC-MS as described by Borisjuk et al. (2013a) with some modifications. Frozen embryos were homogenized in 2-mL microcentrifuge tubes (Eppendorf) containing two steel beads (ASK) by grinding in a Retsch TissueLyser (Qiagen) for 45 s at 1,800 strokes min^{-1}. After homogenization, the samples were extracted with precooled ($-20°C$) 0.5 mL of 2:3 (v/v) methanol:chloroform and 0.1 mL of methanol added with 5 nmol of acephate as an internal standard (solution at room temperature) under the same grinding conditions. Then, 0.3 mL of water was added to achieve two layers, followed by centrifugation at 2,000g for 5 min at 4°C. The main part of the upper water/methanol layer (approximately 0.4 mL) was filtered with Vivaclear centrifugal filters (0.8 μm pore size; SatoriusStedim Biotech) at 2,000g for 2 min at 4°C. The extract was distributed in three aliquots. Three different methods were used to determine metabolite concentrations.

An ion chromatograph (ICS-3000 system; Dionex) was coupled to a triple quadrupole mass spectrometer (ABSciex) in negative mode. The injection volume was 10 μL. The separation was performed on an IonSwift MAX-100 (1 × 250 mm; Dionex) device with a constant column temperature of 40°C and a column flow of 150 $\mu L\ min^{-1}$. The suppressor was set to a value of 38 mV. As sodium hydroxide eluent, we used the following gradient: 0 min (7 mM), 6.5 min (7 mM), 22 min (60 mM), 24 min (100 mM), 28.5 min (100 mM), 30 min (7 mM), and 40 min (7 mM).

The other methods applied hydrophilic interaction chromatography and were performed with the coupling of the liquid chromatograph (Ultimate 3000; Dionex) and the same mass spectrometer. To obtain a maximum of different compounds, the column was used in combination with the mass spectrometer in negative and positive modes and varying eluent gradients, each time using an aminopropyl column (Luna NH2; 250 × 2 mm, particle size of 5 μm; Phenomenex). The injection volume was 2 μL. The LC eluents are as follows: solvent A, 20 mM ammonium acetate + 20 mM ammonium hydroxide in 95:5 water:acetonitrile, pH 9.45; and solvent B, acetonitrile. The gradients in the negative mode are as follows: 0 min, 75% B; 8 min, 70% B; 22 min, 0% B; 32 min, 0% B; 33.5 min, 75% B; and 44 min, 75% B. The gradients in the positive mode are as follows: 0 min, 80% B; 6 min, 75% B; 14 min, 0% B; 24 min, 0% B; 25 min, 80% B; and 35 min, 80% B. Nitrogen was used as a curtain gas, nebulizer gas, heater gas, and collision gas. The ion spray voltage was set to $-4,000$ V, the capillary temperature was 450°C, and the dwell time for all compounds was 25 ms. The MS settings as well as retention times for each metabolite are given by Borisjuk et al. (2013a; Supplemental Table S8A). Compound identities were verified by mass and retention time match to authenticated standards. External calibration was applied using authenticated standards.

Recovery experiments were performed to validate our metabolite data (Supplemental Table S8B). Separate aliquots of the same plant material were extracted in parallel, with or without the addition of known amounts of standards to the frozen plant material prior to extraction. The added standard quantities were adapted to the endogenous amounts and revealed good recoveries (77%–122%). According to Fernie et al. (2011), this indicates a good reproducibility and sensitivity for the metabolites measured in this study.

Calculation of metabolite turnover times (metabolite pool size/rate of synthesis) was based on metabolite quantification and ^{13}C-based MFA flux data. For a quantified metabolic pool, all net fluxes consuming it were summed and equated to the rate of synthesis. For this purpose, metabolite and flux values were converted into the same units (for details, see Supplemental Table S6A).

Proteome Analysis

Proteins were extracted by phenol extraction and separated by two-dimensional isoelectric focusing/SDS gel electrophoresis following the procedure described by Rode et al. (2012). This method is suitable for analyzing soluble and membrane-associated proteins, whereas highly hydrophobic integral membrane proteins are generally underrepresented. Isoelectric focusing was carried out on Immobiline DryStrip gels (24 cm, nonlinear gradient pH 3–11) using the Ettan IPGphor 3 system (GE Healthcare). For the second dimension, the High Performance Electrophorese FlatTop Tower-System (Serva Electrophoresis) was used with precast Tris-Gly gels (12.5% [w/v] polyacrylamide, 24 × 20 cm). First, a reference map was produced with 100 μg of protein from the OSR reference line. The gel was stained overnight with colloidal Coomassie Blue CBB-250 G (Merck), and all visible spots were detected and numbered with Delta2D software version 4.2 (Decodon). Spots were excised with a manual spot picker (Genetix) and analyzed by MS using the EASY-nLC-system (Proxeon) coupled to a MicrOTOF-Q-II mass spectrometer (Bruker Daltonics) as described by Hildebrandt et al. (2013). Proteins were identified with the MASCOT search algorithm against SwissProt (www.uniprot.org) and The Arabidopsis Information Resource 10 (www.arabidopsis.org) and sorted into functional categories according to the information available in these databases. Only proteins identified on the basis of more than one peptide with a MASCOT score of at least 50 were accepted. Proteome comparisons between high- and low-oil lines were achieved with the difference gel electrophoresis minimal labeling technique (CyDye DIGE fluor kit; GE Healthcare). Gels contained 50 μg of protein of each of the two samples and an internal mixed standard produced from all lines. DIGE gels were scanned with a fluorescence scanner (Typhoon Variable Mode Imager 9400; GE Healthcare) and analyzed with Delta2D software version 4.2 (Decodon). Protein spots with significant (Student's t test, $P < 0.05$), at least 1.5-fold differences in the relative spot volume were assumed to be of different abundance and identified via the reference map.

Enzyme Assays

Enzymes were extracted from 20-mg aliquots of frozen ground embryo tissue by vortexing and mixing in 500 μL of common extraction buffer (10% [v/v] glycerol, 0.25% [w/v] bovine serum albumin, 0.1% [v/v] Triton X-100, 50 mM HEPES/KOH, pH 7.5, 10 mM $MgCl_2$, 1 mM EDTA, 1 mM EGTA, 1 mM benzamidine, 1 mM ε-aminocapronic acid, 1 mM phenylmethylsulfonyl fluoride, 10 mM leupeptin, and 1 mM dithiothreitol) and approximately 10 mg of polyvinylpyrrolidone. Phenylmethylsulfonyl fluoride was added just before extraction. Dithiothreitol was omitted when using peroxidase-based or methylthiazolyldiphenyl-tetrazolium bromide-based indicator reactions. A 96-head liquid-handling robot (Evolution P3; Perkin Elmer) was used to perform subsequent dilutions of these initial extracts and to load extracts onto 96-well microplates. During this process, microplates were maintained at 4°C using Peltier cooled blocks. These microplates were then transferred to a second robot platform (Microlab STAR; Hamilton), which enabled simultaneous initiation and termination of reactions in all 96 wells, and an automated incubation station (Automated Hotel; Inheco) enabled controlled incubation of reactions. Reactions were started with the addition of a substrate or cofactor and incubated at 30°C for 20 min. Reactions were then stopped using 0.5 M HCl, 0.5 M NaOH, or 80% (v/v) ethanol. The concentrations of the products of these stopped reactions (NAD^+, NADH, NADPH, or glycerol-3-phosphate) were then determined using cycling assays. The individual stopped assays and the subsequent cycling assays are described in depth elsewhere (Gibon et al., 2002, 2004). Nitrate reductase and Gln synthetase were determined using end-point assays (Gibon et al., 2004). Cytosolic and plastidic activities of pyruvate kinase were assayed based on different pH optima reported before for purified oilseed rape pyruvate kinase isoforms (Plaxton et al., 2002). Accordingly, the cytosolic enzyme has maximum activity at pH 6.7 while the plastidic isoform is inactive. At pH 8, PKp has maximum activity, while PKc has 60% of its activity at pH 6.7. After measuring pyruvate kinase activity at pH 8 and 6.7, the plastidic and cytosolic activities were calculated accordingly.

Histological Procedures

Histochemical techniques applied to seeds were as described earlier (Borisjuk et al., 2005).

Network Analysis and Visualization

The VANTED software (Rohn et al., 2012) was used for correlation analysis and visualization. Pearson correlation between 187 elements (77 metabolites,

26 enzyme activities, and 79 flux values) and the biomass components was determined. For visualization, elements that are significantly correlated to starch or lipid ($R \geq 0.666$) are shown. Color coding of nodes was red (positive correlation) or blue (negative correlation). To further show very strong correlations between elements, including the target, all Pearson correlations with $R \geq 0.9$ were shown as color-coded edges. The strength of the correlation was visualized using edge thickness, where the thickest edges represent a correlation value of 1 and the thinnest edges represent a correlation value of 0.9.

Supplemental Data

The following supplemental materials are available.

Supplemental Figure S1. Biomass composition of an oilseed rape embryo cultured in vitro for 10 d.

Supplemental Figure S2. Visualization of the correlation matrix based on Pearson correlation between biomass components, enzymes, metabolites, and fluxes.

Supplemental Figure S3. Allosteric effects of glycolytic intermediates and their turnover times.

Supplemental Table S1. Biomass composition of in vitro-cultivated embryos from 63 oilseed rape genotypes.

Supplemental Table S2. Biomass composition data of selected oilseed rape entries used for ^{13}C-based MFA.

Supplemental Table S3. ^{13}C-based MFA.

Supplemental Table S4. Enzyme activities measured in various oilseed rape genotypes using the robotized enzyme-profiling platform.

Supplemental Table S5. Metabolite concentrations measured in various oilseed rape genotypes.

Supplemental Table S6. Unit conversion and correlation matrix based on Pearson correlation between biomass components, enzymes, metabolites, and fluxes.

Supplemental Table S7. Proteomics analysis.

Supplemental Table S8. MS detection parameters, chromatographic retention times, and recovery rates of metabolites measured in this study.

Supplemental Methods S1. ^{13}C-based MFA.

ACKNOWLEDGMENTS

LITERATURE CITED

Andre C, Froehlich JE, Moll MR, Benning C (2007) A heteromeric plastidic pyruvate kinase complex involved in seed oil biosynthesis in *Arabidopsis*. Plant Cell 19: 2006–2022

Andriotis VM, Pike MJ, Kular B, Rawsthorne S, Smith AM (2010) Starch turnover in developing oilseed embryos. New Phytol 187: 791–804

Arrivault S, Guenther M, Ivakov A, Feil R, Vosloh D, van Dongen JT, Sulpice R, Stitt M (2009) Use of reverse-phase liquid chromatography, linked to tandem mass spectrometry, to profile the Calvin cycle and other metabolic intermediates in Arabidopsis rosettes at different carbon dioxide concentrations. Plant J 59: 826–839

Baud S, Boutin JP, Miquel M, Lepiniec L, Rochat C (2002) An integrated overview of seed development in *Arabidopsis thaliana* ecotype WS. Plant Physiol Biochem 40: 151–160

Baud S, Lepiniec L (2009) Regulation of de novo fatty acid synthesis in maturing oilseeds of *Arabidopsis*. Plant Physiol Biochem 47: 448–455

Baud S, Lepiniec L (2010) Physiological and developmental regulation of seed oil production. Prog Lipid Res 49: 235–249

Baud S, Wuillème S, Dubreucq B, de Almeida A, Vuagnat C, Lepiniec L, Miquel M, Rochat C (2007) Function of plastidial pyruvate kinases in seeds of *Arabidopsis thaliana*. Plant J 52: 405–419

Baud S, Wuillème S, To A, Rochat C, Lepiniec L (2009) Role of WRINKLED1 in the transcriptional regulation of glycolytic and fatty acid biosynthetic genes in *Arabidopsis*. Plant J 60: 933–947

Belmonte MF, Kirkbride RC, Stone SL, Pelletier JM, Bui AQ, Yeung EC, Hashimoto M, Fei J, Harada CM, Munoz MD, et al (2013) Comprehensive developmental profiles of gene activity in regions and subregions of the *Arabidopsis* seed. Proc Natl Acad Sci USA 110: E435–E444

Borisjuk L, Neuberger T, Schwender J, Heinzel N, Sunderhaus S, Fuchs J, Hay JO, Tschiersch H, Braun HP, Denolf P, et al (2013a) Seed architecture shapes embryo metabolism in oilseed rape. Plant Cell 25: 1625–1640

Borisjuk L, Nguyen TH, Neuberger T, Rutten T, Tschiersch H, Claus B, Feussner I, Webb AG, Jakob P, Weber H, et al (2005) Gradients of lipid storage, photosynthesis and plastid differentiation in developing soybean seeds. New Phytol 167: 761–776

Borisjuk L, Rolletschek H, Neuberger T (2013b) Nuclear magnetic resonance imaging of lipid in living plants. Prog Lipid Res 52: 465–487

Bourgis F, Kilaru A, Cao X, Ngando-Ebongue GF, Drira N, Ohlrogge JB, Arondel V (2011) Comparative transcriptome and metabolite analysis of oil palm and date palm mesocarp that differ dramatically in carbon partitioning. Proc Natl Acad Sci USA 108: 12527–12532

Bridges D, Fraser ME, Moorhead GB (2005) Cyclic nucleotide binding proteins in the *Arabidopsis thaliana* and *Oryza sativa* genomes. BMC Bioinformatics 6: 6

Cassagne C, Lessire R, Bessoule JJ, Moreau P, Creach A, Schneider F, Sturbois B (1994) Biosynthesis of very long chain fatty acids in higher plants. Prog Lipid Res 33: 55–69

Century K, Reuber TL, Ratcliffe OJ (2008) Regulating the regulators: the future prospects for transcription-factor-based agricultural biotechnology products. Plant Physiol 147: 20–29

Cernac A, Andre C, Hoffmann-Benning S, Benning C (2006) WRI1 is required for seed germination and seedling establishment. Plant Physiol 141: 745–757

Cernac A, Benning C (2004) WRINKLED1 encodes an AP2/EREB domain protein involved in the control of storage compound biosynthesis in *Arabidopsis*. Plant J 40: 575–585

Chubukov V, Uhr M, Le Chat L, Kleijn RJ, Jules M, Link H, Aymerich S, Stelling J, Sauer U (2013) Transcriptional regulation is insufficient to explain substrate-induced flux changes in *Bacillus subtilis*. Mol Syst Biol 9: 709

Crevillén P, Ballicora MA, Mérida A, Preiss J, Romero JM (2003) The different large subunit isoforms of Arabidopsis thaliana ADP-glucose pyrophosphorylase confer distinct kinetic and regulatory properties to the heterotetrameric enzyme. J Biol Chem 278: 28508–28515

da Silva PM, Eastmond PJ, Hill LM, Smith AM, Rawsthorne S (1997) Starch metabolism in developing embryos of oilseed rape. Planta 203: 480–487

Durrett TP, Benning C, Ohlrogge J (2008) Plant triacylglycerols as feedstocks for the production of biofuels. Plant J 54: 593–607

Faiz-Ur-Rahman AT, Trewavas AJ, Davies DD (1974) The Pasteur effect in carrot root tissue. Planta 118: 195–210

Farré EM, Tiessen A, Roessner U, Geigenberger P, Trethewey RN, Willmitzer L (2001) Analysis of the compartmentation of glycolytic intermediates, nucleotides, sugars, organic acids, amino acids, and sugar alcohols in potato tubers using a nonaqueous fractionation method. Plant Physiol 127: 685–700

Feher K, Lisec J, Römisch-Margl L, Selbig J, Gierl A, Piepho HP, Nikoloski Z, Willmitzer L (2014) Deducing hybrid performance from parental metabolic profiles of young primary roots of maize by using a multivariate diallel approach. PLoS ONE 9: e85435

Fernie AR, Aharoni A, Willmitzer L, Stitt M, Tohge T, Kopka J, Carroll AJ, Saito K, Fraser PD, DeLuca V (2011) Recommendations for reporting metabolite data. Plant Cell 23: 2477–2482

Fernie AR, Geigenberger P, Stitt M (2005) Flux an important, but neglected, component of functional genomics. Curr Opin Plant Biol 8: 174–182

Fernie AR, Stitt M (2012) On the discordance of metabolomics with proteomics and transcriptomics: coping with increasing complexity in logic, chemistry, and network interactions. Plant Physiol 158: 1139–1145

Finkemeier I, Laxa M, Miguet L, Howden AJM, Sweetlove LJ (2011) Proteins of diverse function and subcellular location are lysine acetylated in Arabidopsis. Plant Physiol 155: 1779–1790

Fischer K, Kammerer B, Gutensohn M, Arbinger B, Weber A, Häusler RE, Flügge UI (1997) A new class of plastidic phosphate translocators: a

putative link between primary and secondary metabolism by the phosphoenolpyruvate/phosphate antiporter. Plant Cell 9: 453–462

Fuchs J, Neuberger T, Rolletschek H, Schiebold S, Nguyen TH, Borisjuk N, Börner A, Melkus G, Jakob P, Borisjuk L (2013) A noninvasive platform for imaging and quantifying oil storage in submillimeter tobacco seed. Plant Physiol 161: 583–593

Gibon Y, Blaesing OE, Hannemann J, Carillo P, Höhne M, Hendriks JH, Palacios N, Cross J, Selbig J, Stitt M (2004) A Robot-based platform to measure multiple enzyme activities in Arabidopsis using a set of cycling assays: comparison of changes of enzyme activities and transcript levels during diurnal cycles and in prolonged darkness. Plant Cell 16: 3304–3325

Gibon Y, Vigeolas H, Tiessen A, Geigenberger P, Stitt M (2002) Sensitive and high throughput metabolite assays for inorganic pyrophosphate, ADPGlc, nucleotide phosphates, and glycolytic intermediates based on a novel enzymic cycling system. Plant J 30: 221–235

Givan CV (1999) Evolving concepts in plant glycolysis: two centuries of progress. Biol Rev Camb Philos Soc 74: 277–309

Goffman FD, Alonso AP, Schwender J, Shachar-Hill Y, Ohlrogge JB (2005) Light enables a very high efficiency of carbon storage in developing embryos of rapeseed. Plant Physiol 138: 2269–2279

Gottlob-McHugh SG, Sangwan RS, Blakeley SD, Vanlerberghe GC, Ko K, Turpin DH, Plaxton WC, Miki BL, Dennis DT (1992) Normal growth of transgenic tobacco plants in the absence of cytosolic pyruvate kinase. Plant Physiol 100: 820–825

Guo L, Ma F, Wei F, Fanella B, Allen DK, Wang X (2014) Cytosolic phosphorylating glyceraldehyde-3-phosphate dehydrogenases affect Arabidopsis cellular metabolism and promote seed oil accumulation. Plant Cell 26: 3023–3035

Gupta M, DeKelver RC, Palta A, Clifford C, Gopalan S, Miller JC, Novak S, Desloover D, Gachotte D, Connell J, et al (2012) Transcriptional activation of Brassica napus β-ketoacyl-ACP synthase II with an engineered zinc finger protein transcription factor. Plant Biotechnol J 10: 783–791

Hajduch M, Hearne LB, Miernyk JA, Casteel JE, Joshi T, Agrawal GK, Song Z, Zhou M, Xu D, Thelen JJ (2010) Systems analysis of seed filling in Arabidopsis: using general linear modeling to assess concordance of transcript and protein expression. Plant Physiol 152: 2078–2087

Hasunuma T, Harada K, Miyazawa S, Kondo A, Fukusaki E, Miyake C (2010) Metabolic turnover analysis by a combination of in vivo ¹³C-labelling from ¹³CO₂ and metabolic profiling with CE-MS/MS reveals rate-limiting steps of the C3 photosynthetic pathway in Nicotiana tabacum leaves. J Exp Bot 61: 1041–1051

Hatzfeld WD, Stitt M (1991) Regulation of glycolysis in heterotrophic cell suspension cultures of Chenopodium rubrum in response to proton fluxes at the plasmalemma. Physiol Plant 81: 103–110

Hay J, Schwender J (2011) Computational analysis of storage synthesis in developing Brassica napus L. (oilseed rape) embryos: flux variability analysis in relation to ¹³C metabolic flux analysis. Plant J 67: 513–525

Hay JO, Shi H, Heinzel N, Hebbelmann I, Rolletschek H, Schwender J (2014) Integration of a constraint-based metabolic model of Brassica napus developing seeds with ¹³C-metabolic flux analysis. Front Plant Sci 5: 724

Hildebrandt TM, Di Meo I, Zeviani M, Viscomi C, Braun HP (2013) Proteome adaptations in Ethe1-deficient mice indicate a role in lipid catabolism and cytoskeleton organization via post-translational protein modifications. Biosci Rep 33: e00052

Junker BH, Lonien J, Heady LE, Rogers A, Schwender J (2007) Parallel determination of enzyme activities and in vivo fluxes in Brassica napus embryos grown on organic or inorganic nitrogen source. Phytochemistry 68: 2232–2242

Kelly AA, Shaw E, Powers SJ, Kurup S, Eastmond PJ (2013) Suppression of the SUGAR-DEPENDENT1 triacylglycerol lipase family during seed development enhances oil yield in oilseed rape (Brassica napus L.). Plant Biotechnol J 11: 355–361

Kim S, Yamaoka Y, Ono H, Kim H, Shim D, Maeshima M, Martinoia E, Cahoon EB, Nishida I, Lee Y (2013) AtABCA9 transporter supplies fatty acids for lipid synthesis to the endoplasmic reticulum. Proc Natl Acad Sci USA 110: 773–778

Kubis SE, Pike MJ, Everett CJ, Hill LM, Rawsthorne S (2004) The import of phosphoenolpyruvate by plastids from developing embryos of oilseed rape, Brassica napus (L.), and its potential as a substrate for fatty acid synthesis. J Exp Bot 55: 1455–1462

Le BH, Cheng C, Bui AQ, Wagmaister JA, Henry KF, Pelletier J, Kwong L, Belmonte M, Kirkbride R, Horvath S, et al (2010) Global analysis of gene activity during Arabidopsis seed development and identification of seed-specific transcription factors. Proc Natl Acad Sci USA 107: 8063–8070

Li X, Gianoulis TA, Yip KY, Gerstein M, Snyder M (2010) Extensive in vivo metabolite-protein interactions revealed by large-scale systematic analyses. Cell 143: 639–650

Lonien J, Schwender J (2009) Analysis of metabolic flux phenotypes for two Arabidopsis mutants with severe impairment in seed storage lipid synthesis. Plant Physiol 151: 1617–1634

Lunn JE, Feil R, Hendriks JH, Gibon Y, Morcuende R, Osuna D, Scheible WR, Carillo P, Hajirezaei MR, Stitt M (2006) Sugar-induced increases in trehalose 6-phosphate are correlated with redox activation of ADP-glucose pyrophosphorylase and higher rates of starch synthesis in Arabidopsis thaliana. Biochem J 397: 139–148

Maeo K, Tokuda T, Ayame A, Mitsui N, Kawai T, Tsukagoshi H, Ishiguro S, Nakamura K (2009) An AP2-type transcription factor, WRINKLED1, of Arabidopsis thaliana binds to the AW-box sequence conserved among proximal upstream regions of genes involved in fatty acid synthesis. Plant J 60: 476–487

Meyer LJ, Gao J, Xu D, Thelen JJ (2012) Phosphoproteomic analysis of seed maturation in Arabidopsis, rapeseed, and soybean. Plant Physiol 159: 517–528

Moraes TF, Plaxton WC (2000) Purification and characterization of phosphoenolpyruvate carboxylase from Brassica napus (rapeseed) suspension cell cultures: implications for phosphoenolpyruvate carboxylase regulation during phosphate starvation, and the integration of glycolysis with nitrogen assimilation. Eur J Biochem 267: 4465–4476

Morandini P (2009) Rethinking metabolic control. Plant Sci 176: 441–451

O'Grady J, Schwender J, Shachar-Hill Y, Morgan JA (2012) Metabolic cartography: experimental quantification of metabolic fluxes from isotopic labelling studies. J Exp Bot 63: 2293–2308

Pickens LB, Tang Y, Chooi YH (2011) Metabolic engineering for the production of natural products. Annu Rev Chem Biomol Eng 2: 211–236

Piques M, Schulze WX, Höhne M, Usadel B, Gibon Y, Rohwer J, Stitt M (2009) Ribosome and transcript copy numbers, polysome occupancy and enzyme dynamics in Arabidopsis. Mol Syst Biol 5: 314

Plaxton WC (1996) The organization and regulation of plant glycolysis. Annu Rev Plant Physiol Plant Mol Biol 47: 185–214

Plaxton WC (2004) Principles of metabolic control. In KB Storey, ed, Functional Metabolism: Regulation and Adaptation. Wiley, Hoboken, NJ, pp 1–24

Plaxton WC, Podestá FE (2006) The functional organization and control of plant respiration. Crit Rev Plant Sci 25: 159–198

Plaxton WC, Smith CR, Knowles VL (2002) Molecular and regulatory properties of leucoplast pyruvate kinase from Brassica napus (rapeseed) suspension cells. Arch Biochem Biophys 400: 54–62

Preiss J (1988) Biosynthesis of starch and its regulation. In J Preiss, ed, The Biochemistry of Plants, Vol 14. Academic Press, San Diego, pp 181–254

Rawsthorne S (2002) Carbon flux and fatty acid synthesis in plants. Prog Lipid Res 41: 182–196

Rode C, Winkelmann T, Braun HP, Colditz F (2012) DIGE analysis of plant tissue proteomes using a phenolic protein extraction method. Methods Mol Biol 854: 335–342

Rohn H, Junker A, Hartmann A, Grafahrend-Belau E, Treutler H, Klapperstück M, Czauderna T, Klukas C, Schreiber F (2012) VANTED v2: a framework for systems biology applications. BMC Syst Biol 6: 139

Rolletschek H, Melkus G, Grafahrend-Belau E, Fuchs J, Heinzel N, Schreiber F, Jakob PM, Borisjuk L (2011) Combined noninvasive imaging and modeling approaches reveal metabolic compartmentation in the barley endosperm. Plant Cell 23: 3041–3054

Ruuska SA, Girke T, Benning C, Ohlrogge JB (2002) Contrapuntal networks of gene expression during Arabidopsis seed filling. Plant Cell 14: 1191–1206

Schwender J (2008) Metabolic flux analysis as a tool in metabolic engineering of plants. Curr Opin Biotechnol 19: 131–137

Schwender J, Goffman F, Ohlrogge JB, Shachar-Hill Y (2004) Rubisco without the Calvin cycle improves the carbon efficiency of developing green seeds. Nature 432: 779–782

Schwender J, Hay JO (2012) Predictive modeling of biomass component tradeoffs in Brassica napus developing oilseeds based on in silico manipulation of storage metabolism. Plant Physiol 160: 1218–1236

Schwender J, König C, Klapperstück M, Heinzel N, Munz E, Hebbelmann I, Hay JO, Denolf P, De Bodt S, Redestig H, et al (2014) Transcript abundance on its own cannot be used to infer fluxes in central metabolism. Front Plant Sci 5: 668

Schwender J, Ohlrogge JB (2002) Probing in vivo metabolism by stable isotope labeling of storage lipids and proteins in developing *Brassica napus* embryos. Plant Physiol 130: 347–361

Schwender J, Ohlrogge JB, Shachar-Hill Y (2003) A flux model of glycolysis and the oxidative pentosephosphate pathway in developing *Brassica napus* embryos. J Biol Chem 278: 29442–29453

Schwender J, Shachar-Hill Y, Ohlrogge JB (2006) Mitochondrial metabolism in developing embryos of *Brassica napus*. J Biol Chem 281: 34040–34047

Singh R, Low ET, Ooi LC, Ong-Abdullah M, Ting NC, Nagappan J, Nookiah R, Amiruddin MD, Rosli R, Manaf MA, et al (2013) The oil palm SHELL gene controls oil yield and encodes a homologue of SEEDSTICK. Nature 500: 340–344

Smith CR, Knowles VL, Plaxton WC (2000) Purification and characterization of cytosolic pyruvate kinase from *Brassica napus* (rapeseed) suspension cell cultures: implications for the integration of glycolysis with nitrogen assimilation. Eur J Biochem 267: 4477–4485

Stitt M, Sonnewald U (1995) Regulation of metabolism in transgenic plants. Annu Rev Plant Physiol Plant Mol Biol 46: 341–368

Sweetlove LJ, Muller-Rober B, Willmitzer L, Hill SA (1999) The contribution of adenosine 5′-diphosphoglucose pyrophosphorylase to the control of starch synthesis in potato tubers. Planta 209: 330–337

Szecowka M, Heise R, Tohge T, Nunes-Nesi A, Vosloh D, Huege J, Feil R, Lunn J, Nikoloski Z, Stitt M, et al (2013) Metabolic fluxes in an illuminated *Arabidopsis* rosette. Plant Cell 25: 694–714

Tang M, Guschina IA, O'Hara P, Slabas AR, Quant PA, Fawcett T, Harwood JL (2012) Metabolic control analysis of developing oilseed rape (*Brassica napus* cv Westar) embryos shows that lipid assembly exerts significant control over oil accumulation. New Phytol 196: 414–426

Theodorou ME, Kruger NJ (2001) Physiological relevance of fructose 2,6-bisphosphate in the regulation of spinach leaf pyrophosphate:fructose 6-phosphate 1-phosphotransferase. Planta 213: 147–157

Theodorou ME, Plaxton WC (1996) Purification and characterization of pyrophosphate-dependent phosphofructokinase from phosphate-starved *Brassica nigra* suspension cells. Plant Physiol 112: 343–351

Thomas S, Mooney PJ, Burrell MM, Fell DA (1997a) Finite change analysis of glycolytic intermediates in tuber tissue of lines of transgenic potato (*Solanum tuberosum*) overexpressing phosphofructokinase. Biochem J 322: 111–117

Thomas S, Mooney PJ, Burrell MM, Fell DA (1997b) Metabolic control analysis of glycolysis in tuber tissue of potato (*Solanum tuberosum*): explanation for the low control coefficient of phosphofructokinase over respiratory flux. Biochem J 322: 119–127

Tiessen A, Hendriks JH, Stitt M, Branscheid A, Gibon Y, Farré EM, Geigenberger P (2002) Starch synthesis in potato tubers is regulated by post-translational redox modification of ADP-glucose pyrophosphorylase: a novel regulatory mechanism linking starch synthesis to the sucrose supply. Plant Cell 14: 2191–2213

Tiessen A, Nerlich A, Faix B, Hümmer C, Fox S, Trafford K, Weber H, Weschke W, Geigenberger P (2012) Subcellular analysis of starch metabolism in developing barley seeds using a non-aqueous fractionation method. J Exp Bot 63: 2071–2087

Troncoso-Ponce MA, Kilaru A, Cao X, Durrett TP, Fan J, Jensen JK, Thrower NA, Pauly M, Wilkerson C, Ohlrogge JB (2011) Comparative deep transcriptional profiling of four developing oilseeds. Plant J 68: 1014–1027

Turner WL, Plaxton WC (2003) Purification and characterization of pyrophosphate- and ATP-dependent phosphofructokinases from banana fruit. Planta 217: 113–121

Vigeolas H, Möhlmann T, Martini N, Neuhaus HE, Geigenberger P (2004) Embryo-specific reduction of ADP-Glc pyrophosphorylase leads to an inhibition of starch synthesis and a delay in oil accumulation in developing seeds of oilseed rape. Plant Physiol 136: 2676–2686

Vigeolas H, van Dongen JT, Waldeck P, Huhn D, Geigenberger P (2003) Lipid storage metabolism is limited by the prevailing low oxygen concentrations within developing seeds of oilseed rape. Plant Physiol 133: 2048–2060

Villadsen D, Nielsen TH (2001) N-terminal truncation affects the kinetics and structure of fructose-6-phosphate 2-kinase/fructose-2,6-bisphosphatase from Arabidopsis thaliana. Biochem J 359: 591–597

Wang N, Shi L, Tian F, Ning H, Wu X, Long Y, Meng J (2010) Assessment of FAE1 polymorphisms in three *Brassica* species using EcoTILLING and their association with differences in seed erucic acid contents. BMC Plant Biol 10: 137

Weitzel M, Nöh K, Dalman T, Niedenführ S, Stute B, Wiechert W (2013) 13CFLUX2: high-performance software suite for ^{13}C-metabolic flux analysis. Bioinformatics 29: 143–145

Weselake RJ, Shah S, Tang M, Quant PA, Snyder CL, Furukawa-Stoffer TL, Zhu W, Taylor DC, Zou J, Kumar A, et al (2008) Metabolic control analysis is helpful for informed genetic manipulation of oilseed rape (*Brassica napus*) to increase seed oil content. J Exp Bot 59: 3543–3549

Wu G, Wu Y, Xiao L, Li X, Lu C (2008) Zero erucic acid trait of rapeseed (Brassica napus L.) results from a deletion of four base pairs in the fatty acid elongase 1 gene. Theor Appl Genet 116: 491–499

Yadav UP, Ivakov A, Feil R, Duan GY, Walther D, Giavalisco P, Piques M, Carillo P, Hubberten HM, Stitt M, et al (2014) The sucrose-trehalose 6-phosphate (Tre6P) nexus: specificity and mechanisms of sucrose signalling by Tre6P. J Exp Bot 65: 1051–1068

Yoo H, Antoniewicz MR, Stephanopoulos G, Kelleher JK (2008) Quantifying reductive carboxylation flux of glutamine to lipid in a brown adipocyte cell line. J Biol Chem 283: 20621–20627

You C, Okano H, Hui S, Zhang Z, Kim M, Gunderson CW, Wang YP, Lenz P, Yan D, Hwa T (2013) Coordination of bacterial proteome with metabolism by cyclic AMP signalling. Nature 500: 301–306
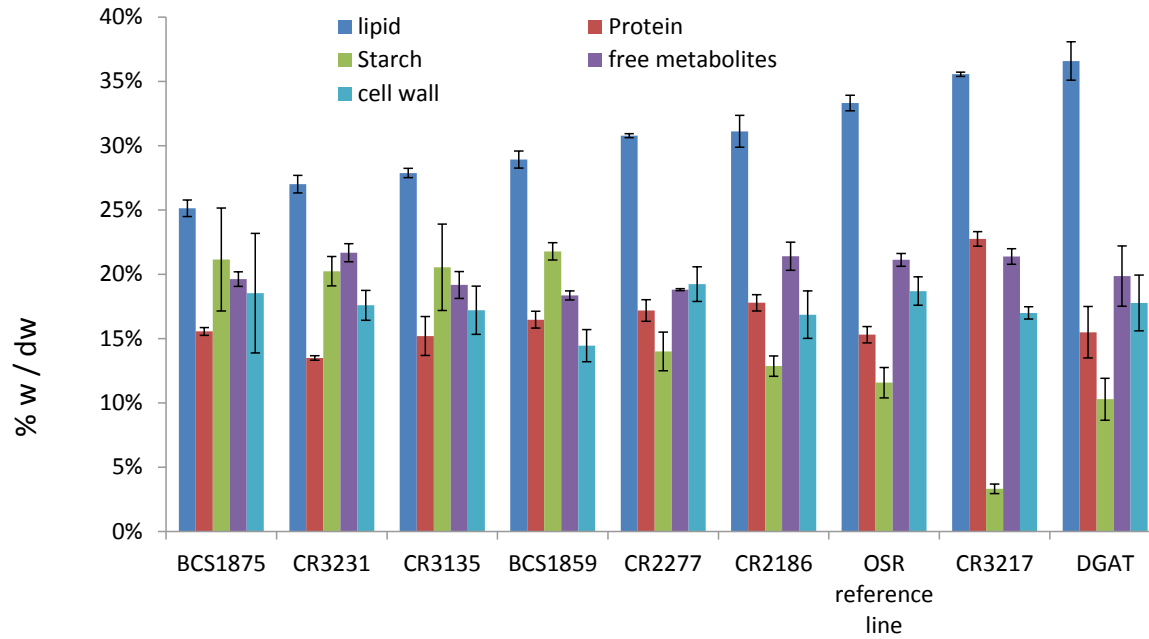
Supplemental Figure S1: Biomass composition of oilseed rape embryo cultured *in vitro* for ten days. See also Supplemental Table S2.
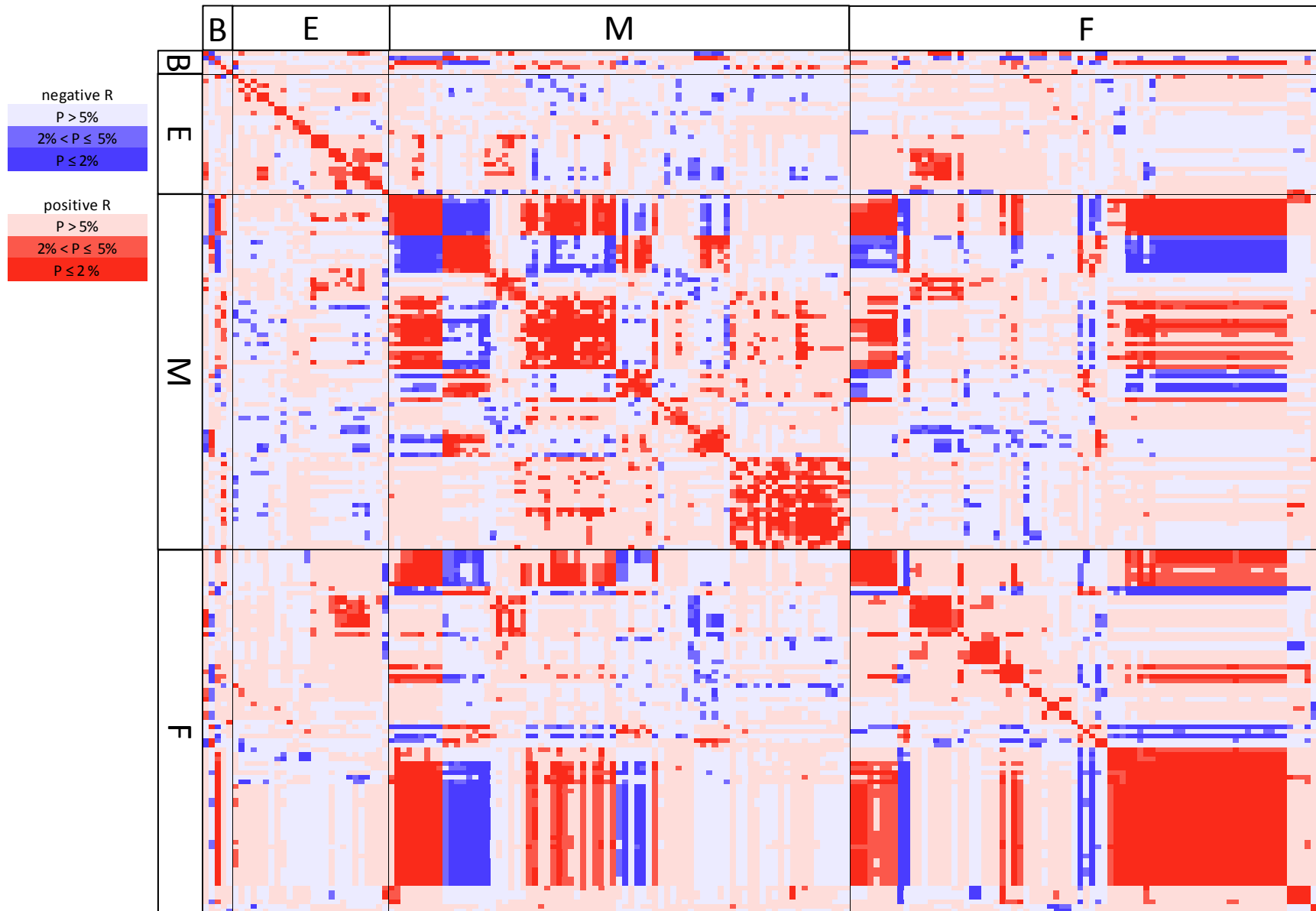
Supplemental Figure S2: Visualization of correlation matrix based on Pearson correlation between biomass components, enzymes, metabolites and fluxes. The original data are given in Supplemental Table S6. For each of the enzymes, metabolites and fluxes datasets the order of observations was sorted based on normalized data and k-means clustering with Euclidian distance measure. Abbreviations: B, biomass components; E, enzyme activities; F, fluxes ; M, metabolites;
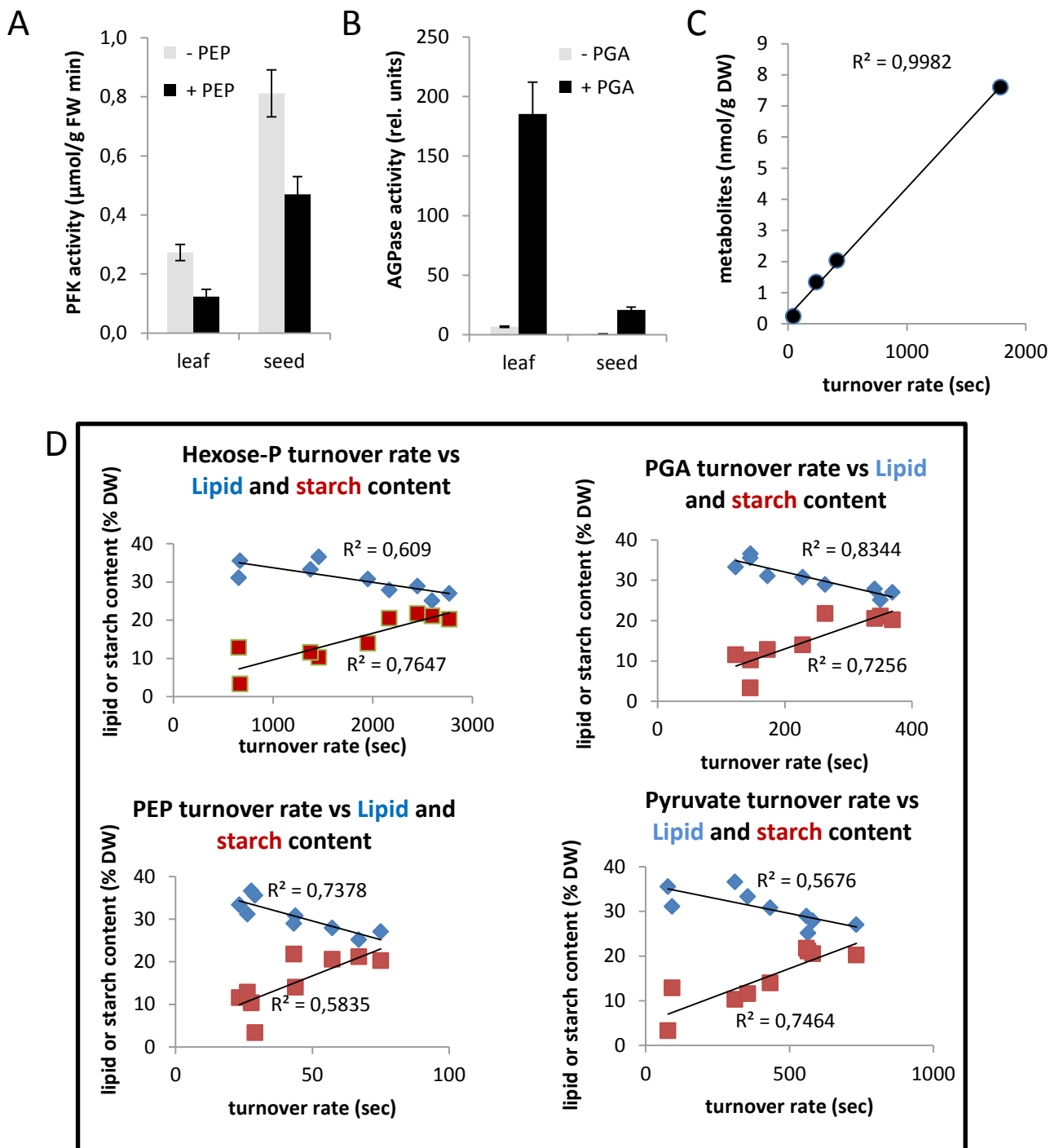
Supplementary Figure S3. Allosteric effects of glycolytic intermediates and their turnover times. (**A,B**) Effect of allosteric regulators on maximum catalytic activity of ATP-dependent phosphofructokinase (PFK) and ADP-glucose pyrophosphorylase (AGPase) measured in tissue extracts of leaf and seed with and without addition of the respective regulators phosphoenolpyruvate (PEP) and 3-phosphoglycerate (3-PGA). Mean values +/- standard deviation are given (n=6). (**C,D**) Calculation of metabolite turnover times based on metabolite quantification and ^{13}C-MFA-based flux data derived in this study for developing oilseed rape embryos. Panel (C) shows the linear relationship between mean concentration of hexose phosphates (sum of glucose-1 phosphate, glucose-6 phosphate, fructose-6 phosphate, and fructose-1,6 diphosphate), PEP, PGA and pyruvate versus mean turnover times; metabolite and flux data were averaged across the genotypes (n=9). Panel (D) shows the turnover time of the same metabolites in relation to either starch (red dots) or lipid (blue dots) content of the individual genotypes. Each dot represents the mean of the individual genotype (n=5). Lines represent regression curves and R^2 gives the corresponding coefficient.

Manuscript Schwender et al.

Supplemental methods File 1 - Experimental details to ^{13}C metabolic flux analysis

Fractionation of embryo material
The fractions of lipid, protein, starch and free metabolites were obtained and quantified as described before in detail (Lonien and Schwender, 2009). In short, after hot extraction using a biphasic solvent system (CHCl$_3$/ methanol/H2O, 8:4:3 v/v; Folch et al., 1957), the DW fractions of lipids, polar compounds and insoluble material (cell pellet) were obtained and quantified by dry weight.

Compositional analysis of biomass fractions
Protein determination was based on elemental analysis of the cell pellet fraction, using a vario MICRO cube CHNS Analyzer in a CHN configuration (Elementar Americas, Mt. Laurel, NJ, USA). The measured weight fraction of nitrogen in the cell pellet fraction was converted into protein by a conversion factor of 5.64 (g protein g^{-1} nitrogen) (Lonien & Schwender, 2009). Starch content in the pellet fraction was determined based on enzymatic degradation as described before in Lonien & Schwender (2009). To determine the fatty acid composition in the lipid fraction, lipids were transesterified and fatty acid methylester quantified by GC-MS (Lonien & Schwender, 2009).
The composition of the fraction of polar compounds was estimated according to independent determination of low molecular polar metabolite composition by LC/MS. Accordingly, in average across all genotypes, 10 metabolites (Sucrose, Gln, Glucose, Pro, ascorbic acid, Arg, citric acid, Glu, Ala, malic acid) account for 95% (weight) of all metabolites quantified by LC/MS (Supplemental table S6). For the modeling process only those most abundant compounds were considered and the about 70 additionally quantified low abundant metabolites were neglected. The relative amounts of the 10 highly abundant polar metabolites were converted into a per *dw* basis based on the total weight of polar compounds determined by biomass fractionation. The biomass composition data used for flux analysis are listed in Supplemental table S2.

Biomass fluxes
The flux model accounts for biomass as the synthesis of 37 metabolite species in 5 main biomass compounds: lipid, protein, starch, cell wall and free metabolites (Supplemental table S2). The fraction of lipid in biomass is accounted as triacylglycerol, with genotype specific composition of nine fatty acid species. Protein is defined uniform for all genotypes according to an approximated abundance of 20 amino acids in seed protein. Starch and cell wall are defined as glucose polymers.
All biomass composition data are given in weight fractions (Supplemental table S2). Biomass compounds (*BC*) can be divided into constituent small molecules, or monomers in case of polymers. For convenience all of these are considered here as "monomer species" (*MS*). For monomer species *i* in a biomass compound *j* we define:

> $MS_{i,j}$, the weight fraction of monomer species *i* in biomass compound *j* (*mg* monomer species / *g* biomass compound),
>   and

BC_j , the weight fraction of biomass compound j in dry weight (mg biomass compound / g dw).

Using the mole mass for monomer species i (Mr_i, g / mol) the molar fraction of monomer i in dry weight can be derived by:

$$MF_i = \frac{\frac{1}{1000}MS_{i,j} \times \frac{1}{1000}BC_j}{Mr_{i,j}} \quad (mol \text{ monomer species} / g\ dw) \qquad \text{(equation 1)}$$

Given a specific growth rate μ (g dw increase / g dw / h), the efflux of the monomer species i is:

$$v_i = \mu MF_i \quad (\text{mol monomer species / mg dw / h}) \qquad \text{(equation 2)}$$

Table SM1. *List of all biomass fluxes derived based on equations 1 and 2. For simplicity of the metabolic network, various biomass fluxes combine the drain of multiple very similar monomer species.*

Biomass flux	Network metabolite	monomer species accounted for by drain of network metabolite
vAlaP	Ala	Ala into protein, free Ala
vAsxP	Asp	Asp, Asn into protein, free malate
vCit_out	Cit	free citrate
vFAEc	AcCoAc	cytosolic fatty acid elongation, export of acetate units
vFASp	AcCoAp	plastidic fatty acid synthesis, export of acetate units
vGlc_out	Hex	Free sucrose
vGlnP	Gln	Gln into protein, free metabolite Gln
vGluP	Glu	Glu, Pro, Arg into protein and free metabolites Glu, Pro, Arg
vGlyc_outa	TPc	glycerol part of TAG (symmetric metabolite, two different carbon transitions)
vGlyc_outb	TPc	glycerol part of TAG (symmetric metabolite, two different carbon transitions)
vGlyP	Gly	Gly into protein
vHisP	His	His, Trp into protein, biosynthesis only rudimentary implemented as drain of ribose 5-phosphate (RPp) and one-carbon intermediate (C1).
vIleP	Ile	Ile into protein
vLeuP	Leu	Leu into protein
vLysP	Lys	Lys into protein
vPheP	Phe	Phe into protein
vSerP	Ser	Ser, Cys into protein
vThrP	Thr	Thr, Met into protein
vTyrP	Tyr	Tyr into protein
vValP	Val	Val into protein
vHPc_out	HPc	drain of cytosolic hexosephospate into cell wall
vSt_out	HPp	drain of plastidic hexosephosphate into starch

Fluxes were further converted into the units *mmol /l /h* based on the following conversion factors: (1) the density of embryo tissue was determined to be approximately 1.2 *mg fw / ml*. (2) The ratio of *fw* to *dw* ratio is approximately 2. (3) By microscopic studies (data not shown) an estimated 33% of the volume of the embryo tissue is metabolically active (Supplemental Table 5E).

Mass spectrometric analysis of labeling signatures
Analysis of isotope enrichment was done with an Agilent 6890N GC coupled to an Agilent 5975 quadrupole mass spectrometer (Agilent Technologies). As described in detail before (Lonien and Schwender, 2009) the following metabolites were analyzed across all nine genotypes: T-butyl-dimethylsilyl derivatives of amino acids derived from hydrolysis of cell pellet fraction (27 fragments in 12 amino acids). Glycerol derived from transmethylation of triacylglycerols (lipid fraction) was analyzed as trifluoroacetate derivative (2 fragments). Glucose derived from starch (cell pellet) was analyzed as glucose methoxime penta-acetate (2 fragments). After hydrogenation of the lipid-derived fatty acid methyl esters, saturated fatty acid methyl esters were analyzed (2 fragments in C18 and C20). The fraction of free polar metabolites was derivatized as methoxyamine-trimethylsilyl derivatives, and sucrose-(trimethylsilyl)$_8$ and citric acid-(trimethylsilyl)$_4$ were analyzed (1 fragment each).

All mass isotopomer measurements were made based on single ion monitoring. Mass spectral data were extracted using the ChemStation Program (MSD ChemStation; Agilent Technologies). In addition to the labeled samples, unlabeled standards were analyzed to verify fragment purity. In similar as described by Antoniewicz et al. (2007) unlabeled and uniformly labeled references were analyzed and the measured isotopomer peak abundances where compared to the abundances expected by known isotope composition of the fragments. Fragments with deviation of > 1 mol % in any mass isotopomer fractions were rejected. For the 35 confirmed molecular fragments analysis of the ^{13}C-labeling experiments was done and the contribution of naturally occurring isotopes in the derivative side chains was corrected for as reported before (Lonien and Schwender, 2009).

Statistical uncertainty in MS measurements
For each genotype four parallel embryo cultures were analyzed resulting in four datasets. The corrected mass isotopomer distribution was determined in 35 confirmed molecular fragments for the four experimental replicates of each genotype. Across the genotypes the standard deviations (SD) in 1575 corrected mass isotopomer fractions ranged from 0.0004% to 0.7% (% fractional enrichment scale), with 90% of the SD values <0.25% and 99% of the SD values <0.5%. Instrumental accuracy was also assessed by repeated analysis of unlabeled amino acid standards and the absolute difference between theoretical and measured mass isotopomer fractions ranged between 10^{-6}% and 0.95% (% fractional enrichment scale). Since these differences were in many cases larger than the experimental standard deviations, it was decided to replace all original experimental SD values < 0.5% with a uniform value of 0.5%. This definition of statistical uncertainty was applied for flux parameter fitting and for additional statistical analysis (Monte Carlo sampling).

Model structure

The structure of the ^{13}C-MFA model is according to Hay et al. (2014).

Subcellular resolution of flux: It has been demonstrated before that fluxes through plastidic and cytosolic pyruvate kinase reactions can be quantitatively resolved in *B. napus* embryo cultures (Schwender et al., 2006, Lonien and Schwender, 2009). This was based on determination of an additional model constraint, derived from quantification of the reversibility of the cytosolic inter-conversion of Ala and pyruvate (vAT.xch) based on feeding ^{15}N-Ala (Schwender et al., 2006). In the present study vAT.xch was set to a fixed value of 250 for all models, which brings Ala_c and $pyruvate_c$ to isotopic equilibration. Considering the absolute scale in fluxes, this is equivalent to the value formerly applied for *B. napus* embryo cultures (Schwender et al., 2006).

Flux parameter fitting

Flux parameter fitting was performed using the 13CFLUX2 toolbox (Weitzel et al., 2013) on a linux cluster (Brookhaven Linux Cluster) under Scientific Linux 5 (Supplemental tables 3B, 3F, 3G). For all nine genotype models flux parameter fitting was performed by multi-start optimization using 13CFLUX2 selecting the optimization library IPOPT (https://projects.coin-or.org/Ipopt). Fluxes were determined by a search algorithm that predicts 175 MS measurements in 34 MS fragments (measurement groups) based on variation of 14 free net fluxes and 28 free exchange fluxes and minimizes the difference between measured and predicted MS measurements as the sum of squares of standard deviation weighted differences (sum of squared residuals, SSR). As described before in detail, one of the free net flux parameters allows the model to adjust for the dilution of biomass components by unlabeled preexisting biomass (Lonien and Schwender, 2009). For each genotype, optimization was started 400 times starting with uniformly distributed random flux distributions and ended if an iteration limit of 2000 was reached. The best fit of a model was defined as a repeatedly obtained minimal SSR. Across the nine genotypes the SSR ranged between 41 and 108. The flux model has 102 degrees of the freedom (175 MS signals -14 free net fluxes -25 free exchange fluxes -34 MS fragments). For 102 degrees of freedom the $\chi2$ critical value is 120.68 (α=0.1). For the 400 random start points in each model, in about 30% cases the optimization runs ended with a SSR smaller than the critical value and for each genotype the 10 best optimized flux sets were inspected to assess how well flux values were reproduced by the optimization. For each flux the scattering of randomized start values was compared to the scattering of optimized values based on standard deviation. Across the 9 genotypes, this value was reduced between 10 and 4000 times, except for the three free net fluxes vTPT, vGPT, vPPT. Therefore we conclude that across the genotypes the best fit flux sets were consistently reproduced with respect to most fluxes except the three ones.

For the best flux sets the goodness of fit was inspected for all particular measured MS fragments, across all genotypes. Initially the labeling signatures for fragment C20_12 could only be fit well for the models CR3231, CR2277 and CR3217, while the residuals were outstandingly high for the other six genotypes. C20_12 relates to label in the terminal acetate unit of C20 fatty acids and the six genotypes where this fragment doesn't fit well are those with only minimal amounts of fatty acids with chain length > 18 carbon.

This is a specific quality trait found in many *B. napus* cultivars, which has been attributed a defect in the cytosolic fatty acid chain elongation, causing erucic acid and other fatty acids > 18 carbons chain length to be almost completely absent in seed oil (Katavic et al., 2002; Wu et al., 2008). The inability of the model to fit the label in C20_12 points to a different biosynthetic origin of the terminal biosynthetic acetate units in C20. In the model the cytosolic elongation of fatty acids is derived from citrate via cytosolic acetyl-CoA derived from ATP:citrate lyase. Apparently, if the cytosolic chain elongation is defect, minimal amounts of C20 and C22 fatty acids are synthesized from another source. Since the fragment C20_12 does only represent a very low flux in the low erucic acid lines, these models were further analyzed by leaving out the C20_12 measurements.

Flux statistics
The statistical uncertainty in the best fit flux values was assessed based on random re-sampling of the MS data and flux measurements according to Gaussian distribution (Box and Muller, 1958) and re-optimization from random start values for the free fluxes. For each genotype this Monte Carlo approach was repeated 10 times (each time 50 random starts) and the resulting 10 best fit flux vectors were used to calculate standard deviations for all fluxes.

Flux scaling of genotype specific models
For all genotypes, the original flux parameter fitting and statistical evaluation was done by scaling the model based on equation 2 by using the specific growth rate $\mu = 0.014$ *mg dw increase / mg dw / h* formerly determined for *B. napus* embryos growing under the same conditions (Schwender et al., 2006). Such a definition of a uniform growth rate is most convenient for comparison of flux values across the genotypes. However, at day 10 in culture, when embryos were harvested for analysis, differences in embryo *dw* of up to two-fold indicated genotype specific differences in growth rates (Supplemental Table S3E). Therefore the flux distributions should be at different scales for the different genotypes. In the following we describe an embryo specific growth model that allows estimating genotype specific growth rates at day 10 in culture. Applying these to the flux models results in flux pattern that are still in largely in the same scale.

Unless the growth in cultures has a linear kinetics, having data on *dw* at day 10 in culture does not allow to directly derive a growth rate. Since for the present set of experiments we do not have complete growth curves for all genotypes (*dw* increase over time), we based the growth kinetics for all genotypes on a formerly established growth curve of *B. napus* (cv. Reston) embryos, grown under the same experimental conditions (Hay and Schwender, 2011). A polynomial fit to measurements of *dw* increase resulted in the following growth function (Hay and Schwender, 2011):

$$dw(t) = -0.0059t^3 + 0.1938t^2 - 0.3649t + 0.6633 \quad \text{(equ. 3)}$$
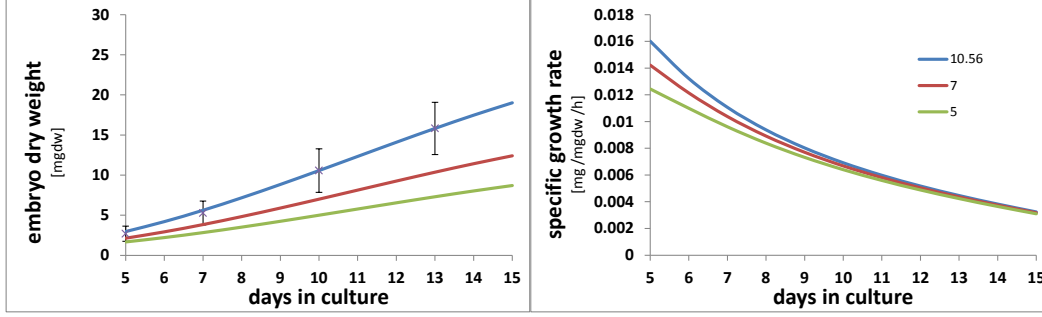
(*dw*, dry weight [*mg*]; *t*, time in culture [*d*])

Figure *SM1*. Kinetics of dry weight accumulation between 5 and 15 days in culture (Hay and Schwender, 2011). A *dw* function was established based on fitting a polynomial to *dw* accumulation data (blue line, equation 3). The curve can be adapted to result in different *dw* at day 10 (red and green lines, equation 5). With reduced steepness in *dw* accumulation, the specific growth rate (equation 7) is reduced. Yet, the largest difference in specific growth rate is expected to be occurring before day 10.

Between about $t = 5$ and $t = 15$ *d*, the *dw* function is continuously increasing. Using the time derivative of equation 3 (*dw(t)'*), the specific growth rate is:

$$\mu = \frac{dw(t)'}{dw(t)} = \frac{-3 \times 0.0059t^2 + 2 \times 0.1938t - 0.3649}{-0.0059t^3 + 0.1938t^2 - 0.3649t + 0.6633} \quad \text{(equ. 4)}$$

This function continuously declines by about 50% between days 6 and 10 (Fig. SM1). Note that for exponential growth the specific growth rate would be constant. However, this decline does not necessarily indicate a strong limitation of growth. The growth in these cultures is not exact cellular replication as possible in the case of unicellular organisms. It is rather a continuous production of storage products.

To estimate growth rates for the different genotypes at day 10 in culture we assumed that cultures of all genotypes grew over the 10 d of culture with similar growth kinetics, i.e. the basic shape of the growth curve should be comparable across the genotypes and we also assume identical size of the starting material. The growth function was modified assuming that differences in *dw* are entirely due to differences in specific growth rates, not to differences in initial *dw*. Accordingly we introduced a constant $\alpha \in [0,1]$ into the *dw* growth function (equation 3) so that *dw*(t=0) is unaffected by α and the slope (time derivative) is reduced at any time point (t > 0) during culture. The modified *dw* function and it's time derivative are:

$$dw(t) = \alpha\left(-0.0059t^3 + 0.1938t^2 - 0.3649t\right) + 0.6633 \text{ (equ. 5)}$$

$$dw(t)' = \alpha(-3 \times 0.0059t^2 + 2 \times 0.1938t - 0.3649) \quad \text{(equ. 6)}$$

Using these modified equations, the specific growth rate is:

6

$$\mu = \frac{dw(t)'}{dw(t)} = \frac{\alpha\left(-3 \times 0.0059t^2 + 2 \times 0.1938t - 0.3649\right)}{\alpha\left(-0.0059t^3 + 0.1938t^2 - 0.3649t\right) + 0.6633} \quad \text{(equ. 7)}$$

Examples of these modified equations 5 and 7 are plotted in Fig. SM2-F1.

In particular, at $t = 10\ d$, equation 5 is:

$$dw(10) = \alpha \times 9.831 + 0.6633 \quad ,$$

which can be re-written as:

$$\alpha = \frac{dw(10) - 0.6633}{9.831}$$

And after substitution of α into equation 6 at t=10 d ($dw(10)' = \alpha \times 1.7411$) we obtain:

$$dw(10)' = \frac{dw(10) - 0.6633}{9.831} \times 1.7411$$

Finally, the specific growth rate at 10 d, dependent on the measured dw is:

$$\mu = \frac{dw(10)'}{dw(10)} = \frac{\dfrac{dw(10) - 0.6633}{9.831} \times 1.7411}{dw(10)}$$

$$= \frac{dw(10) - 0.6633}{9.831 \times dw(10)} \times 1.7411$$

Using above relation and dw data (Supplemental table S3E) the specific growth rate at 10 d can be estimated for each genotype. The values range between 0.1526 and 0.1649 *mg dw increase / mg dw / d*, or 0.00636 and 0.00687 *mg dw increase / mg dw / h* (Supplemental table S3E), indicating that there is only a small variability in growth rates.

References

Box GEP, Muller ME (1958) A note on the generation of random normal deviates. Annals Math. Stat **29:** 610-611

Eicks M, Maurino V, Knappe S, Flügge UI, Fischer K (2002) The plastidic pentose phosphate translocator represents a link between the cytosolic and the plastidic pentose phosphate pathways in plants. Plant Physiology **128:** 512-522

Folch J, Lees M, Sloane Stanley GH (1957) A simple method for the isolation and purification of total lipides from animal tissues. J Biol Chem **226:** 497-509

Hay JO, Schwender J (2011) Metabolic network reconstruction and flux variability analysis of storage synthesis in developing oilseed rape (*Brassica napus* L.) embryos. Plant J **67:** 526–541

Hay JO, Shi H, Heinzel N, Hebbelmann I, Rolletschek H, Schwender J (2014) Integration of a constraint-based model of *Brassica napus* developing seeds with ^{13}C-Metabolic Flux Analysis. Frontiers in Plant Science 5:724

Hutchings D, Rawsthorne S, Emes MJ (2005) Fatty acid synthesis and the oxidative pentose phosphate pathway in developing embryos of oilseed rape (*Brassica napus* L.). Journal of Experimental Botany **56:** 577-585

Katavic V, Mietkiewska E, Barton DL, Giblin EM, Reed DW, Taylor DC (2002) Restoring enzyme activity in nonfunctional low erucic acid Brassica napus fatty acid elongase 1 by a single amino acid substitution. European journal of biochemistry / FEBS **269:** 5625-5631

Lonien J, Schwender J (2009) Analysis of metabolic flux phenotypes for two Arabidopsis mutants with severe impairment in seed storage lipid synthesis. Plant Physiol **151:** 1617-1634

Schwender J, Ohlrogge JB, Shachar-Hill Y (2003) A flux model of glycolysis and the oxidative pentosephosphate pathway in developing *Brassica napus* embryos. Journal of Biological Chemistry **278:** 29442-29453

Schwender J, Shachar-Hill Y, Ohlrogge JB (2006) Mitochondrial metabolism in developing embryos of *Brassica napus*. Journal of Biological Chemistry **281:** 34040-34047

Schwender J (2011) Experimental flux measurements on a network scale. Frontiers in Plant Science **2: article 63**

Tanz SK, Castleden I, Hooper CM, Vacher M, Small I, Millar HA (2013) SUBA3: a database for integrating experimentation and prediction to define the SUBcellular location of proteins in Arabidopsis. Nucleic acids research **41:** D1185-1191

Troncoso-Ponce MA, Kilaru A, Cao X, Durrett TP, Fan J, Jensen JK, Thrower NA, Pauly M, Wilkerson C, Ohlrogge JB (2011) Comparative deep transcriptional profiling of four developing oilseeds. The Plant journal **68:** 1014-1027

Weitzel M, Noh K, Dalman T, Niedenfuhr S, Stute B, Wiechert W (2013) 13CFLUX2--high-performance software suite for 13C-metabolic flux analysis. Bioinformatics **29:** 143-145

Wu G, Wu Y, Xiao L, Li X, Lu C (2008) Zero erucic acid trait of rapeseed (Brassica napus L.) results from a deletion of four base pairs in the fatty acid elongase 1 gene. TAG. Theoretical and applied genetics. Theoretische und angewandte Genetik **116:** 491-499